

Copyright Warning & Restrictions

The copyright law of the United States (Title 17, United States Code) governs the making of photocopies or other reproductions of copyrighted material.

Under certain conditions specified in the law, libraries and archives are authorized to furnish a photocopy or other reproduction. One of these specified conditions is that the photocopy or reproduction is not to be “used for any purpose other than private study, scholarship, or research.” If a user makes a request for, or later uses, a photocopy or reproduction for purposes in excess of “fair use” that user may be liable for copyright infringement,

This institution reserves the right to refuse to accept a copying order if, in its judgment, fulfillment of the order would involve violation of copyright law.

Please Note: The author retains the copyright while the New Jersey Institute of Technology reserves the right to distribute this thesis or dissertation

Printing note: If you do not wish to print this page, then select “Pages from: first page # to: last page #” on the print dialog screen

The Van Houten library has removed some of the personal information and all signatures from the approval page and biographical sketches of theses and dissertations in order to protect the identity of NJIT graduates and faculty.

ABSTRACT

EFFICIENT INVERSION METHODS IN UNDERWATER ACOUSTICS

by
Xiaoqun Ma

This dissertation describes efficient methods developed and implemented for source localization and sound speed and bottom depth estimation using sound propagation in the ocean. The proposed inversion techniques are based on the linearization of the generally non-linear inverse problem of parameter estimation in underwater acoustics. These techniques take into account properties of the ocean environment and are accurate in their estimation results without being prohibitively computationally intensive. For the inversion, select ray paths are taken into account: the direct, first surface bounce, and first bottom bounce. Ray travel time derivatives with respect to parameters that affect path arrival times are obtained analytically. These derivatives and a first order expansion are then used to find estimates of unknown parameters through replica and true paths; replica paths are generated using ray theory for underwater sound propagation and true paths are identified from measured time series. The linearization scheme works efficiently for the estimation of geometric parameters such as the source and receiver location coordinates and the depth of the water column. It is also successful in estimating the sound speed profile in the ocean using empirical orthogonal functions. In this work, the linearization inversion technique is applied to marine mammal tracking, and it is also used with real data collected during the Haro Strait experiment for source and receiver localization. For the Haro Strait data, inversion using linearization is also compared to matched-field processing, which estimates source location and geoacoustic parameters through a full field matching approach.

**EFFICIENT INVERSION METHODS
IN UNDERWATER ACOUSTICS**

by
Xiaoqun Ma

**A Dissertation
Submitted to the Faculty of
New Jersey Institute of Technology
and Rutgers, The State University of New Jersey–Newark
in Partial Fulfillment of the Requirements for the Degree of
Doctor of Philosophy in Mathematical Sciences**

**Department of Mathematical Sciences
Department of Mathematics and Computer Science, Rutgers–Newark**

May 2001

Copyright © 2001 by Xiaoqun Ma

ALL RIGHTS RESERVED

APPROVAL PAGE

**EFFICIENT INVERSION METHODS
IN UNDERWATER ACOUSTICS**

Xiaoqun Ma

4/25/01

Dr. Zoi-Heleni Michalopoulou, Dissertation Advisor
Associate Professor of Mathematical Sciences, NJIT

Date

4/25/01

Dr. David C. Stickler, Committee Member
Professor of Mathematical Sciences, NJIT

Date

4/25/01

~~Dr.~~ Jonathan H. C. Luke, Committee Member
Associate Professor of Mathematical Sciences, NJIT

Date

4/25/01

~~Dr.~~ Bonnie K. Ray, Committee Member
Associate Professor of Mathematical Sciences, NJIT

Date

4/25/01

Dr. Hongya Ge, Committee Member
Assistant Professor of Electrical and Computer Engineering, NJIT

Date

4/25/01

Dr. Alex Tolstoy, Committee Member
ATolstoy Sciences

Date

BIOGRAPHICAL SKETCH

Author: Xiaoqun Ma
Degree: Doctor of Philosophy
Date: May 2001

Undergraduate and Graduate Education:

- Doctor of Philosophy in Mathematical Sciences,
New Jersey Institute of Technology, Newark, NJ, 2001
- Master of Science in Applied Mathematics,
New Jersey Institute of Technology, Newark, NJ, 1998
- Bachelor of Engineering in Engineering Mechanics,
Shanghai Jiao Tong University, Shanghai, P. R. China, 1988

Major: Applied Mathematics

Publications:

- Z. H. Michalopoulou, X. Ma, M. Picarelli, U. Ghosh-Dastidar,
“Fast Matching Methods for Inversion with Underwater Sound”,
Proceedings of Oceans 2000 MTS/IEEE Conference, Providence, Rhode Island,
September, 2000
- X. Ma, Z. H. Michalopoulou,
“Model based time delay processing for underwater source localization and tracking”,
Proceedings of Fifth European Conference on Underwater Acoustics ECUA
2000, Lyon, France, July, 2000
- X. Ma, Z. H. Michalopoulou,
“Matched arrival processing for efficient inversion in underwater acoustics”,
Proceedings of Oceans '99 MTS/IEEE Conference, Seattle, Washington,
September, 1999

Awards:

Office of Naval Research (ONR) Graduate Traineeship Award, 1999

To my sweetheart and dear parents

ACKNOWLEDGMENT

I would like to express my deepest gratitude to Dr. Zoi-Heleni Michalopoulou. She has been a great mentor to me throughout my academic career in NJIT. Without her inspiration and enthusiasm, this work would be an impossible mission. Not only her precise perspective but also her ardent spirit has given me the desire to make things right, to excel myself in all areas.

My gratitude also goes to Dr. Ahluwalia. Through all these years, he has created an atmosphere of self-discipline which built the momentum for this work.

There is no enough words to express my appreciation to Dr. Luke, Dr. Stickler, Dr. Ray, Dr. Ge, and Dr. Tolstoy for serving as members of my dissertation committee. It is their precious advice and suggestions that finally makes this work complete. I am also indebted to Dr. Stan Dosso for his invaluable help and Dr. Ross Chapman for providing the Haro Strait data and references.

I sincerely thank all faculty members and staff for their constant encouragement and support, especially Dr. Bechtold, Dr. Blackmore, Dr. Booty, Ms. Gulati, and Ms. Sutton. It is truly a privilege working with every one of you and you make me feel “rich”.

I also want to thank all my friends for their endless help and friendship.

My heartfelt thanks must go to my family-my parents, and especially my wife. I can never be the person I can be if her love, understanding and belief are taken away from my life. *Into each life some rain must fall, some days be dark and dreary.* But with you, I can always see the sunshine.

This work is supported by Office of Naval Research (ONR) through grant number N000140010051.

TABLE OF CONTENTS

Chapter	Page
1 INTRODUCTION	1
2 UNDERWATER SOUND PROPAGATION	4
2.1 The Acoustic Wave Equation	5
2.2 Numerical Models for the Solution of the Wave Equation	6
2.3 Ray Theory	7
3 INVERSION USING LINEARIZATION	10
3.1 The Inverse Component	10
3.2 The Environment	10
3.3 The Linear System	12
3.4 Ray Travel Time Derivatives	14
3.5 Ray Parameter Evaluation	16
3.5.1 Newton's Method	17
3.5.2 Bisection	18
3.6 Numerical Methods for the Solution of the Linear System	20
3.6.1 Least Squares	21
3.6.2 Regularization Method	22
4 INVERSION WITH SYNTHETIC DATA	25
4.1 General Configuration	25

TABLE OF CONTENTS
(Continued)

Chapter	Page
4.2 Inversion for Source Parameters	26
4.2.1 Inversion with Arrival Times Known Exactly	26
4.2.2 Inversion with Uncertain Arrival Times	30
4.3 Inversion for Source Parameters in an Uncertain Environment	35
4.3.1 Inversion Sensitivity to Receiver Depth	36
4.3.2 Inversion Sensitivity to Ocean Bottom Depth	37
4.3.3 Ocean Bottom Depth Inversion	38
4.4 Including Receiver Depths in the Inversion Process	42
5 INVERSION FOR SOUND SPEED PROFILE	45
5.1 Localization under the Assumption of an Isovelocity Sound Speed Profile	45
5.2 Sensitivity of Source Localization to Sound Speed Uncertainty	46
5.3 Sound Speed Profile Inversion	47
5.3.1 EOF Model	47
5.3.2 Inversion without Temporal Noise	48
5.3.3 Inversion with Uncertain Arrival Times	49
6 INVERSION WITH REAL DATA	56
6.1 Haro Strait Experiment	56
6.2 Localization Results	57

TABLE OF CONTENTS
(Continued)

Chapter	Page
6.2.1 Reference Data	57
6.2.2 NE Data	58
6.2.3 NW Data	61
6.2.4 SW Data	65
7 MATCHED FIELD INVERSION WITH THE HARO STRAIT DATA	68
8 OCEAN MAMMAL TRACKING	72
8.1 Description of the Tracking Approach	72
8.2 Tracking Results Using Synthetic Data	73
9 CONCLUSIONS	76
APPENDIX A THE DERIVATION OF ARRIVAL TIME DERIVATIVES ALONG RAY PATHS	78
APPENDIX B THE DERIVATION OF ARRIVAL TIME DERIVATIVES FOR SOUND SPEED COEFFICIENT	81
APPENCIX C THE DERIVATION OF ARRIVAL TIME DERIVATIVES FOR RANGE DEPENDENT ENVIRONMENT	84
APPENDIX D COORDINATES CONVERSION BETWEEN GEODETIC SYSTEM AND CARTESIAN SYSTEM	89
REFERENCES	90

LIST OF TABLES

Table	Page
4.1 Source localization employing arrival times along three ray paths.	27
4.2 Source localization with different initial conditions and ray paths.	28
4.3 Source localization results using the linearized approach with relative times.	29
4.4 Source localization with five receivers using different initial conditions and ray paths and relative times.	30
4.5 Source localization results with different arrival time uncertainties.	32
4.6 Source localization results with different arrival time uncertainties using relative arrival times.	34
5.1 Source localization results using a constant sound speed profile in the three path case.	45
5.2 Source localization results under sound speed uncertainty in the three path case with relative arrival times known exactly.	47
5.3 Sound speed profile data for EOF model	49
6.1 Source localization using LS - NE array.	60
6.2 Source localization using regularization - NE array.	60
6.3 Source localization using LS - NW array.	62
6.4 Source localization using regularization - NW array.	62
6.5 Mean and standard deviation of localization parameters from Jaschke's method - NW array.	63
6.6 Sound speed profile data for sound speed inversion - NW array	64

Table	Page
6.7 Source localization with uncertain sound speed - NW array.	65
6.8 Receiver location estimation - NW array.	65
6.9 Source localization using LS - SW array.	67
6.10 Source localization using regularization - SW array.	67
8.1 Rms tracking errors using different paths. The standard deviation for the arrival time uncertainty is 0.1 ms.	74
8.2 Rms tracking errors using different paths. The standard deviation for the arrival time uncertainty is 1 ms.	75

LIST OF FIGURES

Figure	Page
1.1 Arrivals in the ocean impulse response.	2
2.1 Forward and inverse mapping.	5
2.2 Impulse response of sound propagation in the ocean.	9
3.1 The propagation geometry.	11
3.2 Different geometric shapes of the direct ray path.	15
3.3 Using bisection to evaluate the ray parameter.	19
4.1 Sound speed profile for synthetic data	25
4.2 Ray trace plot of sound speed propagation.	26
4.3 Histograms calculated from Monte Carlo simulations for source localization using absolute arrival times: (a) source range in two path case; (b) source depth in two path case; (c) source range in three path case; (d) source depth in three path case.	31
4.4 Histograms calculated from Monte Carlo simulations for source localization using relative arrival times: (a) source range in two path case; (b) source depth in two path case; (c) source range in three path case; (d) source depth in three path case.	33
4.5 Monte Carlo simulations for source localization using relative arrival times: (a) scatter plots of depth vs. range in two path case; (b) scatter plots of depth vs. range in three path case.	34
4.6 Monte Carlo simulations for source coordinate inversion using relative arrival times and introducing an error in one receiver depth: (a) histogram of source range; (b) histogram of source depth.	36

Figure	Page
4.7 Monte Carlo simulations for source coordinates inversion using relative arrival times and introducing an error in bottom depth: (a) histogram of source range; (b) histogram of source depth.	37
4.8 Monte Carlo simulations for source and bottom parameters inversion using absolute arrival times and three paths: (a) histogram of source range (b) histogram of source depth (c) histogram of bottom depth . . .	38
4.9 Histograms calculated from Monte Carlo simulations for source and bottom parameters inversion using relative arrival times and three paths: (a) histogram of source range (b) histogram of source depth (c) histogram of bottom depth.	39
4.10 Histograms calculated from Monte Carlo simulations for source and bottom parameters inversion using regularization and relative arrival times: (a) histogram of source range (b) histogram of source depth (c) histogram of bottom depth.	40
4.11 Results from Monte Carlo simulations for source and receiver parameters inversion using relative arrival times and three ray paths with known receiver depth: (a) scatter plot using the least squares method with bottom depth known exactly; (b) scatter plot using the least squares method with bottom depth unknown; (c) scatter plot using the regularization method with bottom depth unknown.	41
4.12 Monte Carlo simulations for source range and bottom depth inversion using relative arrival times and three ray paths: (a) scatter plots using least squares method; (b) scatter plots using regularization method. . .	42
4.13 Monte Carlo simulations for source and receiver parameter inversion using regularization and relative arrival times: (a) histogram of source range (b) histogram of source depth (c) histogram of top receiver depth.	43
4.14 Monte Carlo simulations for source and receiver location and bottom depth inversion through regularization with relative arrival times and three ray paths: (a) histogram of source range (b) histogram of source depth (c) histogram of receiver depth (d) histogram of bottom depth. .	44
5.1 Sound-speed profile mismatch	46
5.2 Measured and mean sound speed profile data.	48

Figure	Page
5.3 Histograms calculated from Monte Carlo simulations for source localization and sound speed coefficient estimation using three ray paths and absolute arrival times: (a) histogram of source range (b) histogram of source depth (c) histogram of sound speed coefficient.	50
5.4 Histograms calculated from Monte Carlo simulations for source localization and sound speed coefficient estimation using three ray paths and relative arrival times: (a) histogram of source range (b) histogram of source depth (c) histogram of sound speed coefficient.	51
5.5 Histograms from Monte Carlo simulations for source localization using regularization with three ray paths and relative arrival times (0.5 ms temporal noise): (a) histogram of source range (b) histogram of source depth (c) histogram of bottom depth (d) histogram of top receiver depth (e) histogram of sound speed coefficient.	53
5.6 Histograms from Monte Carlo simulations for source localization using regularization with three ray paths and relative arrival times (1 ms temporal noise): (a) histogram of source range (b) histogram of source depth (c) histogram of bottom depth (d) histogram of top receiver depth (e) histogram of sound speed coefficient.	54
5.7 Histograms from Monte Carlo simulations for source localization using regularization with three ray paths and relative arrival times (2 ms temporal noise): (a) histogram of source range (b) histogram of source depth (c) histogram of bottom depth (d) histogram of top receiver depth (e) histogram of sound speed coefficient.	55
6.1 A sketch of the Haro Strait experiment.	57
6.2 Locations of the light bulbs and hydrophone arrays.	58
6.3 Raw light bulb pressure signals, recorded at the NE-array.	59
6.4 Raw light bulb pressure signals, recorded at the NW-array.	61
6.5 “Measured” and mean sound speed profile - NW array.	63
6.6 Sound speed profile estimation using EOF model.	64
6.7 Raw light bulb pressure signals, recorded at the SW-array.	66

Figure	Page
7.1 Assumed acoustic environment for MFP.	69
7.2 Arrival time series recorded in Haro Strait - NW site.	70
7.3 Matched-field processing results for three different sites.	71
8.1 Clicks generated from a vocalizing marine mammal (provided by Centro Interdisciplinare di Bioacustica of the University of Pavia, Italy).	73
8.2 Source tracking using relative arrival times with two paths.	74
A.1 Sound propagation through infinitesimal isovelocity layers.	78
C.1 Bottom bounce ray path in slope bottom case.	84

CHAPTER 1

INTRODUCTION

Inverse theory plays a critical role in underwater acoustics for the estimation of geometric parameters (source and receiver location, bottom depth) and environmental parameters (sound speed profiles, sediment densities, attenuations and sediment layer depths).

A popular approach for inversion in underwater acoustics is matched-field processing [1, 2, 3]. Inversion of the acoustic field using matched-field processing techniques requires a combination of wave propagation modeling for the generation of replica fields at receiving phones and a decision rule that estimates the unknown parameters. Values of the unknown parameters that maximize the similarity between replica and true acoustic fields are the desired estimates.

Matched-field processing has been used with excellent results both on synthetic and real data ([3, 4, 5, 6, 7, 8, 9]). However, as a full-field matching approach, this method typically requires that the full acoustic field is calculated at a set of receiving phones and is matched to the received acoustic data. Thus, many parameters enter the estimation process. Although we might only be interested in estimating the source location, many factors need to be taken into consideration such as the water column depth and the properties of the bottom sediment, for example, since those affect the full field. Uncertainty regarding these parameters has to be incorporated in the estimation process for accurate inversion. Therefore, the computational load of matched-field inversion methods could be substantial, especially when the number of the unknown parameters is large and the signal carries broadband information.

In order to avoid multiple replica field calculation, many attempts have been made to investigate the potential for matching only select features of the acoustic

field to corresponding replica features. For example, different inversion methods have been performed using distinct arrival times ([10, 11, 12, 13]). Also fast linearization schemes have been successfully implemented in several aspects of inversion in underwater acoustics and seismic studies ([4, 14, 15, 16, 17, 18]). More specifically, linearized inversion comparing direct path arrival times at spatially separated phones was demonstrated in [13] and [16] with excellent results in array element localization. Linearization for acoustic inversion using arrival times, however, requires identification of the nature of each arrival observed in the ocean impulse response (that is, how many bounces (if any) each path has gone through and with which interfaces it has interacted). Such identification is not always straightforward, especially when only limited prior information is available on the propagation environment.

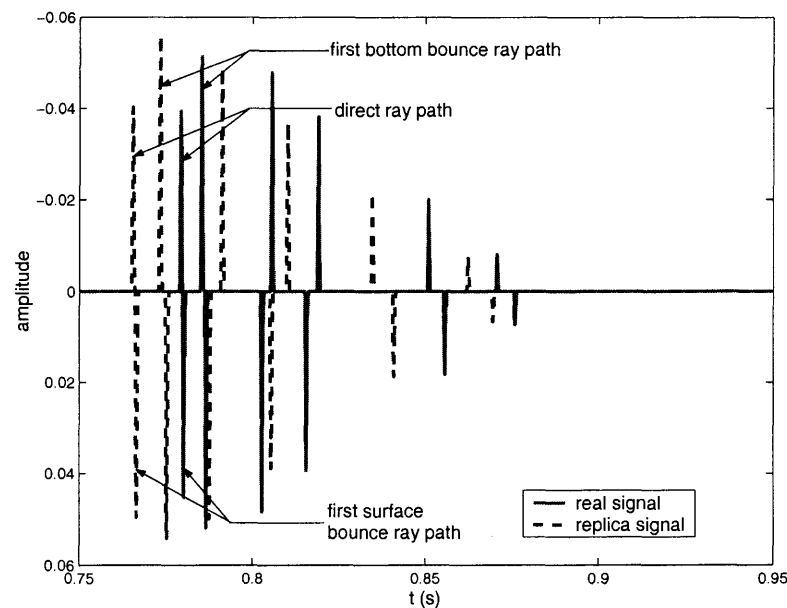


Figure 1.1 Arrivals in the ocean impulse response.

In this dissertation, a linearization inversion method is developed that employs select ray paths (the direct, first surface bounce, and first bottom bounce ray path, for example) for source localization and bottom depth and sound speed parameter estimation. The specific paths were selected in this work, because they are usually

simple to identify. Often, the direct path is the first detected arrival, the first surface bounce path is the arrival that follows the direct arrival with its sign different from that of the direct path, a result of the reflection at the surface; whereas the first bottom bounce path is the arrival that follows the direct arrival with the same direction as the direct path arrival. This sign/phase difference is illustrated in Figure 1.1. In essence, the proposed method is a localization approach through model-based time-delay estimation, which compares the arrival times of the aforementioned paths to theoretically predicted arrival times for paths of the same nature. The latter arrival times, which are also referred to here as replica arrival times, are generated using ray theory for different values of the unknown parameters. Similarly to matched-field processing, our estimates are those values that maximize the match between measured and replica path arrival times.

The structure of this dissertation is as follows: Chapter 2 discusses acoustic wave propagation models used in forward modeling involved in source and ocean parameter estimation problems. Chapter 3 presents the linearized inversion method. Chapter 4 presents and discusses results from the application of the method to synthetic data for source and receiver localization and bottom depth estimation. Chapter 5 implements the method for sound speed estimation using empirical orthogonal functions. Chapter 6 demonstrates the application of the linearization method to the Haro Strait data set for source localization. Chapter 7 discusses matched-field processing results from the same data. Chapter 8 shows how marine mammal tracking can be achieved using linearized inversion. The results of this dissertation are summarized in Chapter 9. Chapter 9 also includes suggestions and directions for future research.

CHAPTER 2

UNDERWATER SOUND PROPAGATION

Solving an inverse problem involves two components, the forward and the inverse models. The forward model provides us with a mathematical relationship between the unknown parameters that need to be estimated and, in our case, the acoustic field. The inverse model determines the rule that will be used for the calculation of the unknown parameters given the data (that is, the measured acoustic field) and the forward mathematical relationship.

To illustrate the structure of an inverse problem, it is assumed that there are N data measurements, forming vector \mathbf{d} :

$$\mathbf{d} = [d_1, d_2, \dots, d_N]^T. \quad (2.1)$$

It is also assumed that there are M unknown parameters m_1, m_2, \dots, m_M forming vector \mathbf{m} :

$$\mathbf{m} = [m_1, m_2, \dots, m_M]^T. \quad (2.2)$$

Here, $[.]^T$ denotes transpose.

The forward model allows us to predict \mathbf{d} for different combinations of the components of vector \mathbf{m} . The inverse model identifies the values of the components of \mathbf{m} that give the best prediction of \mathbf{d} . Figure 2.1 illustrates the process involved in the solution of our inverse problem.

The present section focuses on the forward component of our problem, which is here a model for sound propagation in the ocean. Underwater sound propagation is mathematically described by the acoustic wave equation, whose parameters and boundary conditions relate directly to the ocean environment, the source and receiver location, and the frequency content of the propagating sound. Here, the

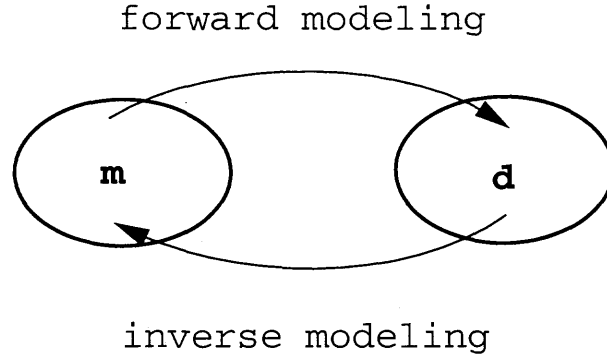


Figure 2.1 Forward and inverse mapping.

wave equation is described briefly and the most common numerical approaches to its solution are presented. Ray theory is emphasized in particular, since it is the main approach in this dissertation for solving the forward problem.

2.1 The Acoustic Wave Equation

The acoustic wave equation can be derived from the mass conservation law, Newton's Second Law, and the adiabatic relation between pressure and density ([19]):

$$\rho \nabla \cdot \left(\frac{1}{\rho} \nabla p \right) - \frac{1}{c^2} \frac{\partial^2 p}{\partial t^2} = 0. \quad (2.3)$$

Here, c is the sound speed in the acoustic environment; ρ is the fluid density; and p is pressure.

For constant density, Equation 2.3 becomes:

$$\nabla^2 p - \frac{1}{c^2} \frac{\partial^2 p}{\partial t^2} = 0. \quad (2.4)$$

Equation 2.4 describes acoustic wave propagation in the time domain. Equation 2.4 can be simplified through a mapping from the time domain to the frequency domain. The trade-off is the evaluation of Fourier transforms for the mapping between the two domains.

In the frequency domain, Equation 2.4 leads to Helmholtz Equation:

$$\nabla^2 p + k^2 p = 0. \quad (2.5)$$

Here, p is pressure (dependent on space and radial frequency ω), and k is the wavenumber, which is defined as the ratio between frequency and sound speed:

$$k = \frac{\omega}{c}. \quad (2.6)$$

For further information on the wave equation, we refer the reader to [19, 20].

2.2 Numerical Models for the Solution of the Wave Equation

There are essentially five different numerical models for approaching the forward problem of acoustic propagation [19]:

- Ray theory

Ray theory provides a high-frequency asymptotic solution to the wave equation. The approximation leads to simple ordinary differential equations in ray coordinates that can be easily solved. The ray method is capable of providing important information on sound propagation without calculating the whole wavefield evolution. Ray theory is computationally efficient and its relationship to geometry makes it simple to follow and understand.

- Wavenumber integration

The wavenumber integration technique involves the application of integral transforms to the wave equation for horizontally stratified media. Another term used to refer to this method is Fast Field Programs because of the use of FFTs for integral calculations in some implementations. Wavenumber integration presents stability challenges and is computationally demanding.

- Normal modes

The normal mode method uses separation of variables to solve the Helmholtz equation, from which the modal equation is derived. The modal equation has an infinite number of solutions (modes); the complete acoustic field is constructed by summing up scaled contributions of the depth-dependent modes. Normal mode models can be extended for the study of range dependent problems using coupled modes or the adiabatic approximation. Implementing the coupled mode approach is particularly computationally intensive.

- Parabolic equation (PE)

The approach starts with the Helmholtz equation and, using Hankel functions in its solution, arrives at the parabolic wave equation. The method is particularly attractive in range dependent situations.

- Finite difference and finite element models

Finite difference and finite element models solve the wave propagation equation through direct discretization techniques, which are capable of solving the two-way wave equation in inhomogeneous fluid-elastic environments with complex geometry. These methods are cumbersome to implement from a computational point of view; they are mostly used when effects from boundary scattering need to be incorporated in a sound propagation problem.

2.3 Ray Theory

Ray models have been used for many years in underwater acoustics [19, 20, 21]. They are fast and can calculate the acoustic field fairly accurately especially in high frequency situations, when other models become computationally demanding.

Ray theory is derived by looking for an asymptotic solution for the Helmholtz equation (in cartesian coordinates):

$$\nabla^2 p + k^2(\mathbf{x})p = 0. \quad (2.7)$$

The asymptotic solution, referred to as the ray series, is in the form:

$$p(\mathbf{x}) = e^{i\omega\tau(\mathbf{x})} \sum_{j=0}^{\infty} \frac{A_j(\mathbf{x})}{(i\omega)^j}. \quad (2.8)$$

By substituting the ray series into the Helmholtz equation and neglecting higher order terms (high-frequency approximation), two equations are obtained:

$$|\nabla\tau|^2 = c^{-2}(\mathbf{x}), \quad (2.9)$$

$$2\nabla\tau \cdot \nabla A_0 + (\nabla^2\tau)A_0 = 0. \quad (2.10)$$

Equation 2.9 for the phase function $\tau(\mathbf{x})$ is called the eikonal equation and Equation 2.10 for amplitude $A_0(\mathbf{x})$ is named the transport equation.

The eikonal equation is a first-order nonlinear PDE. It can be simplified using the method of characteristics, leading to a linear ODE:

$$\frac{d\tau}{ds} = \frac{1}{c}, \quad (2.11)$$

where s is the arc length along the ray path. Equation 2.11 defines the travel time along the ray path, which can be written as:

$$\tau = \int_S^R \frac{1}{c(s)} ds. \quad (2.12)$$

The transport equation can also be simplified to a linear ODE:

$$\frac{2}{c} \frac{dA_0}{ds} + (\nabla^2\tau)A_0 = 0. \quad (2.13)$$

Integration of this ODE leads to the solution for A_0 .

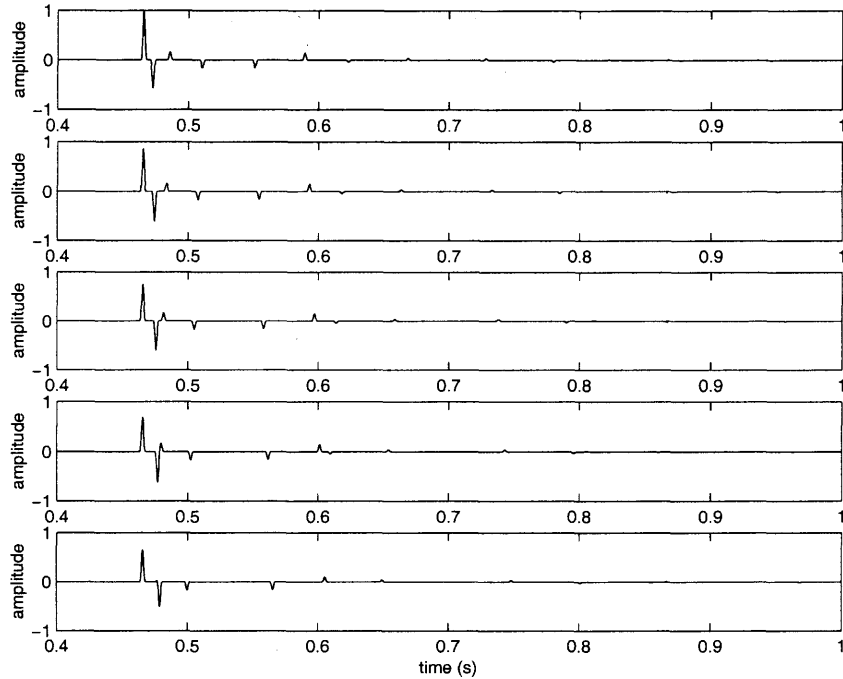


Figure 2.2 Impulse response of sound propagation in the ocean.

In this work, sound propagation using ray theory was performed using BELLHOP [22] and code written by the author. Figure 2.2 shows the impulse response of the ocean calculated with BELLHOP for a shallow water propagation environment. The impulse response is calculated at five receiving phones (the top impulse response corresponds to the shallowest phone). Peaks of the impulse response correspond to the arriving paths that are used for inversion.

CHAPTER 3

INVERSION USING LINEARIZATION

In this chapter, the kernel of this work is presented: a linearization approach to the non-linear inverse problem of parameter estimation in underwater acoustics. A linear system is set up relating time delays between path arrivals and the parameters that need to be estimated. Time delays and unknown parameters are linked through derivatives of ray arrival times with respect to the parameters. Different approaches are discussed for the solution of the linear system for better estimation of the parameters of interest.

3.1 The Inverse Component

In Chapter 2, forward modeling was discussed, from which the acoustic field in the ocean can be mathematically expressed given a specific underwater environment and source and receiver location. Using observed data and a selected forward model, we now want to “invert” in order to find the source location which resulted in the generation of an observed acoustic field (data). Using the notation of Chapter 2, the inversion process can be described as:

$$\mathbf{d} \implies \mathbf{f} \implies \mathbf{m}$$

3.2 The Environment

The ocean is an acoustic waveguide limited above by the sea surface and below by the seafloor. In this work, a shallow water, range-independent environment and a broadband, high-frequency source are considered. Ray theory is used to model propagation between source and receivers [19]. Short range propagation is addressed, in order for the ray paths of interest (direct, surface and bottom paths) to be resolvable.

The received fields are measured at several, vertically separated receiving phones. A sketch of the problem geometry is shown in Figure 3.1.

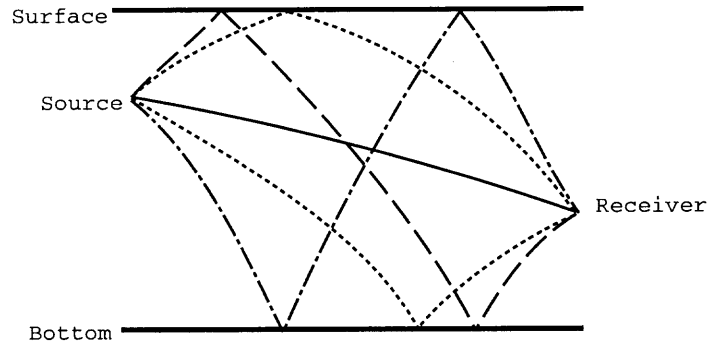


Figure 3.1 The propagation geometry.

The sound speed plays a critical role in acoustic wave propagation, as shown from the wave equation (2.4). Sound speed is here treated as constant with range, but it varies as a function of depth. The ray paths follow Snell's Law,

$$\frac{\sin \theta}{c(z)} = p = \text{constant}, \quad (3.1)$$

where θ is the ray incident angle, $c(z)$ is the depth dependent sound speed, and p is defined as the ray parameter which remains constant along each specific ray path. This implies that a ray path bends locally toward regions of low sound speed. The importance of the sound speed profile to the inversion model is represented in detail in the following chapters.

The paths employed in this work for inversion were selected, because they are usually simple to identify through the arrival order and sign/phase differences, as mentioned in Chapter 1. Furthermore, the direct and first surface bounce paths do not interact with the ocean bottom. Acoustic inversion using only these paths can, thus, be achieved without involving potentially complicated and unknown bathymetry. If the bathymetry is well known, however, the information can be

introduced into the localization process improving the results; introduction of bathymetry information can be achieved through the use of paths that have been reflected off the seafloor. Those paths could be also used for bathymetry estimation, as will be shown latter.

3.3 The Linear System

The arrival time t of each specific ray path depends on the geometry and environmental parameters of the underwater problem of interest: source range r , source depth z_s , receiving phone depths z_r , bottom (water column) depth D , sound speed profile $c(z)$, and the source instant t_0 . For the present, the sound speed profile is assumed to be known; the arrival time of a path can be written as:

$$t = \tau(r, z_s, z_r, D) + t_0, \quad (3.2)$$

where τ represents the ray travel time.

Here the single source case is considered, while the signal is received at multiple hydrophones. For an array with N hydrophones, if three characteristic ray paths (direct, first surface bounce, first bottom bounce) are employed, there will be a total of $3N$ arrival time measurements (data) which depend on $2N + 3$ parameters (two spatial variables for each hydrophone, source depth, bottom depth, and time instant). Using the notation of Chapter 2, these measurements can be described as

$$\mathbf{d} = \mathbf{f}(\mathbf{m}), \quad (3.3)$$

where \mathbf{d} is the vector of measured travel times ($\mathbf{d} = \mathbf{t}$); \mathbf{f} represents the forward method, or acoustic model, that relates the measurements to a set of parameters; \mathbf{m}

represents the vector of these parameters:

$$\mathbf{m} = [r_i, z_s, z_{r,i}, D, t_0], \quad i = 1, 2, \dots, N. \quad (3.4)$$

For the acoustic inverse problem, vector \mathbf{m} is estimated using the measured travel times and forward model \mathbf{f} . The inverse process is nonlinear. An effective approach to the nonlinear inverse process is local linearization and iteration. The linear approximation to Equation 3.3 can be obtained through a Taylor expansion to the leading order about an arbitrary initial vector \mathbf{m}_0 ([13, 17, 18]):

$$\mathbf{d} = \mathbf{f}(\mathbf{m}_0) + \mathbf{J}\delta\mathbf{m}, \quad (3.5)$$

where $\delta\mathbf{m}$ is the model perturbation, and \mathbf{J} is the Jacobian matrix which contains the time derivatives with respect to each of the unknown parameters along specific ray paths. By introducing $\delta\mathbf{t} = \mathbf{d} - \mathbf{f}(\mathbf{m}_0)$, Equation 3.5 yields

$$\mathbf{J}\delta\mathbf{m} = \delta\mathbf{t}. \quad (3.6)$$

Equation 3.6 reflects a linear relationship between arrival times and the parameters in \mathbf{m} .

The time differences $\delta\mathbf{t}$ of Equation 3.6 are measured between path arrivals in the real signals and replica signals generated using ray theory for a set of initial values for the unknown parameters. Through Equation 3.6, corrections $\delta\mathbf{m}$ for the unknown parameters are obtained, that give a better match between real and replica times. Depending on the proximity between initial values of the parameters and the noise level in the arrival times, the system might need to be solved iteratively several times until it converges.

Equation 3.6 generally leads to an overdetermined linear system. Different methods for the solution of this system are presented and compared in this work.

3.4 Ray Travel Time Derivatives

The linearization approach requires the computation of ray travel time derivatives with respect to the unknown parameters. The derivation of the time derivatives with respect to source and receiver locations for the direct ray path is presented analytically in [13]. The approach of [13] is extended in this work for all the geometric parameters along each characteristic ray path.

The time derivatives with respect to source range r , source depth z_s , receiver depth z_r , and bottom depth D are calculated in the following way:

For the direct ray path:

$$\frac{\partial t}{\partial r} = p, \quad (3.7)$$

$$\frac{\partial t}{\partial z_s} = -\frac{\sqrt{1 - p^2 c^2(z_s)}}{c(z_s)}, \quad (3.8)$$

$$\frac{\partial t}{\partial z_r} = \frac{\sqrt{1 - p^2 c^2(z_r)}}{c(z_r)}, \quad (3.9)$$

$$\frac{\partial t}{\partial D} = 0. \quad (3.10)$$

For the first surface-bounce ray path:

$$\frac{\partial t}{\partial r} = p, \quad (3.11)$$

$$\frac{\partial t}{\partial z_s} = \frac{\sqrt{1 - p^2 c^2(z_s)}}{c(z_s)}, \quad (3.12)$$

$$\frac{\partial t}{\partial z_r} = \frac{\sqrt{1 - p^2 c^2(z_r)}}{c(z_r)}, \quad (3.13)$$

$$\frac{\partial t}{\partial D} = 0. \quad (3.14)$$

For the first bottom-bounce ray path:

$$\frac{\partial t}{\partial r} = p, \quad (3.15)$$

$$\frac{\partial t}{\partial z_s} = -\frac{\sqrt{1 - p^2 c^2(z_s)}}{c(z_s)}, \quad (3.16)$$

$$\frac{\partial t}{\partial z_r} = -\frac{\sqrt{1 - p^2 c^2(z_r)}}{c(z_r)}, \quad (3.17)$$

$$\frac{\partial t}{\partial D} = \frac{2\sqrt{1 - p^2 c^2(D)}}{c(D)}. \quad (3.18)$$

Here, $c(z)$ is the sound speed at depth z . The ray parameter p , as defined in Equation 3.1, characterizes rays connecting source and receiver (eigenrays).

Notice that the expression for $\frac{\partial t}{\partial r}$ is the same for different ray paths. Also there are only sign differences for both $\frac{\partial t}{\partial z_s}$ and $\frac{\partial t}{\partial z_r}$ between the surface and bottom reflected path calculations. The derivation of these travel time derivatives is further described in Appendix A.

In fact, along each characteristic ray path, time derivatives $\frac{\partial t}{\partial z_s}$ and $\frac{\partial t}{\partial z_r}$ may change sign due to the geometric shape of the path. This can be further illustrated through an example of a particular direct ray path.

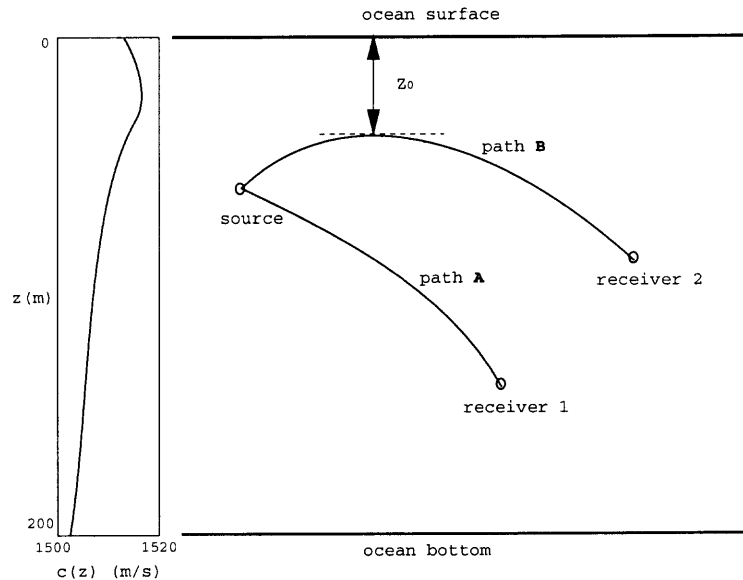


Figure 3.2 Different geometric shapes of the direct ray path.

Path **A** in Figure 3.2 is a typical direct ray path between source and receiver 1, for which the source range r is described as

$$r = \int_{z_s}^{z_r} \frac{pc(z)}{\sqrt{1 - p^2c^2(z)}} dz. \quad (3.19)$$

The time derivatives $\frac{\partial t}{\partial z_s}$ and $\frac{\partial t}{\partial z_r}$ follow Equations 3.8 and 3.9.

However, the direct ray path **B** between source and receiver 2 is a bell shaped path. In this case, the equation for the source range r should be presented as

$$r = \int_{z_0}^{z_s} \frac{pc(z)}{\sqrt{1 - p^2c^2(z)}} dz + \int_{z_0}^{z_r} \frac{pc(z)}{\sqrt{1 - p^2c^2(z)}} dz. \quad (3.20)$$

This equation for range is similar to that of range for the surface bounce ray path, which implies that both $\frac{\partial t}{\partial z_s}$ and $\frac{\partial t}{\partial z_r}$ are positive along the path.

Therefore, in practice, the geometric properties of each ray path must be investigated thoroughly using appropriate prior knowledge of the environment. This is important for accurate estimation of the ray parameter, which plays a key role in the time derivative computation. In the next section, different numerical approaches are presented for ray parameter evaluation.

3.5 Ray Parameter Evaluation

Calculations of ray travel derivatives require the knowledge of ray parameter p . According to Snell's Law, p remains constant along each ray path. Newton's method is suggested for the evaluation of p for the direct ray path in [13]. This method can also be applied for both the surface bounce and bottom bounce ray paths. Due to restrictions of this method, a bisection method is also implemented.

3.5.1 Newton's Method

Using Newton's method, the ray parameter can be evaluated iteratively in the following way ([13]):

$$p_{i+1} = p_i + \left[\frac{\partial r(p_i)}{\partial p} \right]^{-1} (r(p) - r(p_i)). \quad (3.21)$$

Here r is described as a function depending on p_i ; $r(p)$ is the known range between the receiver and source of the replica signal.

Along the first surface bounce ray path, the source range r can be expressed as a function of p using Snell's Law:

$$r = \int_0^{z_s} \frac{pc(z) dz}{\sqrt{1 - p^2 c^2(z)}} + \int_0^{z_r} \frac{pc(z) dz}{\sqrt{1 - p^2 c^2(z)}}. \quad (3.22)$$

Using this equation, $\partial r / \partial p$ can be derived as follows:

$$\frac{\partial r}{\partial p} = \int_0^{z_s} \frac{c(z) dz}{[1 - p^2 c^2(z)]^{3/2}} + \int_0^{z_r} \frac{c(z) dz}{[1 - p^2 c^2(z)]^{3/2}}. \quad (3.23)$$

For the first surface reflection, the initial value p_0 is obtained by assuming straight-line propagation from the source to the ocean surface and from the surface to the receiver with sound speed c_H , where:

$$c_H = \max\left(z_s / \int_0^{z_s} \frac{dz}{c(z)}, \quad z_r / \int_0^{z_r} \frac{dz}{c(z)}\right). \quad (3.24)$$

The maximum value of the two terms is selected in order for Snell's Law to hold for the entire ray path. By definition, p_0 can be written as:

$$p_0 = \frac{r}{c_H \sqrt{r^2 + (z_s + z_r)^2}}. \quad (3.25)$$

For the replica signal, ray parameter p can be obtained from iterations of Equation 3.21, until $r(p)$ is approached by $r(p_i)$ within a desired tolerance.

This ray parameter estimation scheme is very efficient due to the fast convergence of Newton's method; it takes only a few iteration steps to get good results. The method can be extended for the first bottom bounce ray path calculations in a straightforward manner.

Given an arbitrary sound speed profile, both integral Equations 3.22 and 3.23 need to be evaluated numerically (using Simpson's method, for example). Especially when the ray parameter p is very small, high precision is required for the integral estimation. Solution of Equations 3.22 and 3.23 can be, however, facilitated if the sound speed profile is treated as a piece-wise linear function of depth. Under this condition, the integral equations can be evaluated explicitly. The following example illustrates the process.

Assuming that sound speed $c(z)$ is a linear function of z :

$$c(z) = az + b, \quad z \in [z_1, z_2], \quad z_1 \leq z_2 \quad (3.26)$$

leading to:

$$r = \int_{z_1}^{z_2} \frac{pc(z)}{\sqrt{1 - p^2c^2(z)}} dz = \frac{1}{ap} [\sqrt{1 - p^2c^2(z_1)} - \sqrt{1 - p^2c^2(z_2)}], \quad (3.27)$$

and

$$\frac{\partial r}{\partial p} = \int_{z_1}^{z_2} \frac{c(z)}{[1 - p^2c^2(z)]^{3/2}} dz = \frac{1}{ap^2} \left[\frac{1}{\sqrt{1 - p^2c^2(z_1)}} - \frac{1}{\sqrt{1 - p^2c^2(z_2)}} \right] \quad (3.28)$$

These equations suggest that for the piece-wise linear sound speed profile, r and $\frac{\partial r}{\partial p}$ can be first rewritten as a sum of integrals, which are evaluated term by term using Equations 3.27 and 3.28.

3.5.2 Bisection

The efficiency of Newton's method was discussed in the previous section. However, the method fails in certain cases, as shown in Figure 3.3. A turning point exists on

the direct ray path, at which $pc(z) = 1.0$ and $\frac{\partial r}{\partial p} \rightarrow \infty$ (from Equation 3.23, which was derived for the surface bounce but also applies to a direct path of the form shown in Figure 3.3). Bisection ([23]) is introduced to remedy the problem.

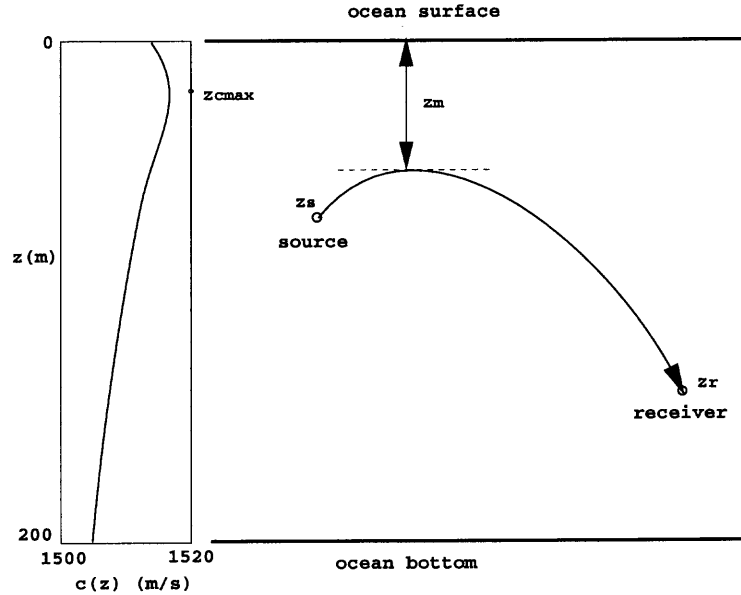


Figure 3.3 Using bisection to evaluate the ray parameter.

To illustrate the approach, we start from an example for the direct ray path of Figure 3.3; it is assumed that $z_s \leq z_r$. Instead of evaluating the ray parameter directly, the depth z_m of the turning point on the path is estimated first using the bisection method. The upper and lower bounds of z_m for the bisection method are determined from the following facts:

- $r(p)$ is a monotonically increasing function of p , since $\frac{\partial r}{\partial p} \geq 0$;
- $p \leq \frac{1}{\max(c(z))}$ holds anywhere on the ray path from Snell's Law.

Thus:

$$z_{c,max} \leq z_m \leq z_s,$$

where $z_{c,max}$ is the depth where $\max(c(z))$ is attained. Starting from this initial interval for z_m , the bisection method for evaluating the ray parameter along the direct ray path can be summarized as follows:

At the i^{th} iteration step, where $z_m \in [z_i, z_{i+1}]$, we have

$$p_i = \frac{1}{c(z_{i+1/2})}, \quad z_{i+1/2} = \frac{z_i + z_{i+1}}{2}, \quad (3.29)$$

$$r_i = \int_{z_s}^{z_{i+1/2}} \frac{p_i c(z)}{\sqrt{1 - p_i^2 c^2(z)}} dz + \int_{z_r}^{z_{i+1/2}} \frac{p_i c(z)}{\sqrt{1 - p_i^2 c^2(z)}} dz. \quad (3.30)$$

By comparing r_i with $r(p)$, the source range for the replica signal, the subinterval for the next iteration step is determined in the following way:

If $r_i > r(p)$, then $z_m \in [z_i, z_{i+1/2}]$;

otherwise, $z_m \in [z_{i+1/2}, z_{i+1}]$.

Similarly to Newton's method, ray parameter value p is obtained when $r(p)$ is approached by $r(p_i)$ within a desired tolerance.

The application of the bisection method to the other ray paths is straightforward. With the numerical schemes described here, it is able to estimate all ray parameters along the ray paths of interest. The time derivatives with respect to the unknown parameters can be then evaluated employing the ray parameter estimates.

3.6 Numerical Methods for the Solution of the Linear System

In this section, different approaches are discussed for solving the linear system of Equation 3.6.

3.6.1 Least Squares

The least squares method solves an inverse problem by finding the parameter values that minimize a particular measure of the length of the estimated data, namely, its Euclidean distance (error) from the observations.

Generally, one could quantify error by different norms. If the error e_i for each observation is defined as the difference between the observed and predicted data, then for N observations:

$$\mathbf{e} = [e_1, e_2, \dots, e_N]. \quad (3.31)$$

The L_n norm for the vector \mathbf{e} is defined as:

$$\|\mathbf{e}\|_n = \left[\sum_{i=1}^N |e_i|^n \right]^{1/n}. \quad (3.32)$$

The goal in estimation is the minimization of the selected error norm. Norm selection is associated with beliefs that we have on the measured data and their accuracy. Minimizing the Euclidean norm for the errors implies the assumption that the data follow Gaussian statistics [17, 18]. In this case, it can be shown that finding the parameter values that maximize the likelihood function formulated under the Gaussian assumption is equivalent to minimizing the errors in a least squares sense. Other norms could be selected when other than Gaussian statistics are believed to govern the errors. When a few outliers in the data are expected to degrade the inversion process significantly, these outliers can be “suppressed” by assuming that the errors have a long-tailed probability distribution. Under this assumption, the outliers will be given little weight (associated with low probability values); as a result, these outliers will not have a substantial effect on the inversion process. Long-tailed probability distribution assumptions for the error correspond to lower order norms. In the case of highly variable data, higher order norms are used, corresponding to probability distributions that assign substantial weight to all data points.

For the linear system of Equation 3.6, the least squares method minimizes quantity χ^2 ([24, 25]), where:

$$\chi^2 = |\mathbf{J}\delta\mathbf{m} - \delta\mathbf{t}|^2. \quad (3.33)$$

Quantity χ^2 is the “misfit” between data and assumptions that needs to be minimized. The solution to Equation 3.33 is obtained by first multiplying Equation 3.6 by \mathbf{J}^T on both sides:

$$\mathbf{J}^T\mathbf{J}\delta\mathbf{m} = \mathbf{J}^T\delta\mathbf{t}, \quad (3.34)$$

leading to:

$$\delta\mathbf{m} = (\mathbf{J}^T\mathbf{J})^{-1}\mathbf{J}^T\delta\mathbf{t}. \quad (3.35)$$

If matrix $\mathbf{J}^T\mathbf{J}$ is not singular, its inverse can be obtained and $\delta\mathbf{m}$ can be easily calculated. However, when the source localization problem includes both the source and receiver positions as unknowns, matrix $\mathbf{J}^T\mathbf{J}$ is usually ill-conditioned, which leads to an ill-posed inverse problem.

3.6.2 Regularization Method

To obtain stable and physical meaningful solutions to the inverse problem of interest, regularization can be employed. This method applies prior information on the unknown parameters to a least squares objective function ([26]).

Setting up the system of Equation 3.35 to solve Equation 3.34 is usually referred to as the creeping approach in inversion: this approach gives the least squares solution for the parameter corrections ($\delta\mathbf{m}$). Since the linear system to be solved is formulated in terms of the parameter perturbations instead of the parameters themselves, a priori information for the parameters cannot be processed directly.

In order for prior information to be included, a different formulation of the linear system can be derived. By introducing vector \mathbf{m}_0 as the vector of initial

conditions for the unknown parameters, Equation 3.6 leads to:

$$\mathbf{Jm} = \mathbf{d} = \mathbf{Jm}_0 + \delta\mathbf{t}. \quad (3.36)$$

Solutions to the linear system of Equation 3.36 give estimates directly for the parameters instead of their corrections (based on initial conditions). The formulation of Equation 3.36 is referred to as the jumping method [13].

To implement regularization, a new objective function α based on the jumping method is minimized. The objective function is defined as ([13]):

$$\alpha = |\mathbf{G}(\mathbf{Jm} - \mathbf{d})|^2 + \lambda|\mathbf{H}(\mathbf{m} - \mathbf{m}_p)|^2, \quad (3.37)$$

where \mathbf{H} is the regularization weighting matrix, including uncertainties on those parameters with available a priori information, and \mathbf{m}_p is the vector containing prior information (estimated mean value) of the components of vector \mathbf{m} . Parameter λ is the Lagrange multiplier. Assuming that the noise for measured data (arrival times) t_i follows a zero mean Gaussian distribution with standard deviation σ_i , \mathbf{G} is a diagonal matrix defined as:

$$\mathbf{G} = \text{diag}[1/\sigma_1, 1/\sigma_2, \dots, 1/\sigma_N]. \quad (3.38)$$

(In our case, $\sigma_1 = \sigma_2 = \dots = \sigma_N$).

The regularized solution is obtained as:

$$\mathbf{m} = (\mathbf{J}^T \mathbf{G}^T \mathbf{G} \mathbf{J} + \lambda \mathbf{H}^T \mathbf{H})^{-1} (\mathbf{J}^T \mathbf{G}^T \mathbf{G} \mathbf{d} + \lambda \mathbf{H}^T \mathbf{H} \mathbf{m}_p). \quad (3.39)$$

Quantity $\lambda \mathbf{H}^T \mathbf{H}$ of Equation 3.39 stabilizes the inversion solution. A search is conducted for a value of λ that will make misfit χ^2 achieve or approach its expected value of N (number of arrival times), which can be expressed as:

$$\chi^2 = N. \quad (3.40)$$

Here χ^2 is defined as:

$$\chi^2 = |\mathbf{G}(\mathbf{f}(\mathbf{m}) - \mathbf{t})|^2, \quad (3.41)$$

where \mathbf{t} is the measured data, vector \mathbf{f} is the forward mapping method (acoustic propagation model), and \mathbf{m} is the vector of estimates of model parameters. Equation 3.41 describes the misfit between the measured data (arrival times) and the data that are generated using the estimated parameters \mathbf{m} and forward mapping method \mathbf{f} .

There are various methods for the formulation of regularization matrix \mathbf{H} based on different a priori information. In this work, \mathbf{H} is selected as:

$$\mathbf{H} = \text{diag}[1/m_1, 1/m_2, \dots, 1/m_M], \quad (3.42)$$

where m_i represents the uncertainty for the i th parameter. For those parameters without a priori information, the corresponding term in \mathbf{H} can be set to zero.

To implement regularization, an arbitrary initial model could be chosen and then solve Equation 3.37 iteratively until convergence is achieved. Convergence is indicated when $\chi^2 = N$. At earlier iterations, χ^2 could obtain very high values (order of 10^6), and finding the right λ to decrease χ^2 could require many iterations. In this work, it was found practical to first use least squares for the calculation of an approximate set of estimates before implementing regularization. The least squares results were used as the initial model for inversion with regularization. Finding values of λ that reduce the χ^2 quantity required only a few iterations in this case, accelerating convergence of the estimation process.

CHAPTER 4

INVERSION WITH SYNTHETIC DATA

In this chapter, a simulation study with synthetic data is carried out for source localization using the linearization approach of Chapter 3. The sensitivity of the inversion results to uncertainties in different parameters (receiver location and bottom depth) is investigated.

4.1 General Configuration

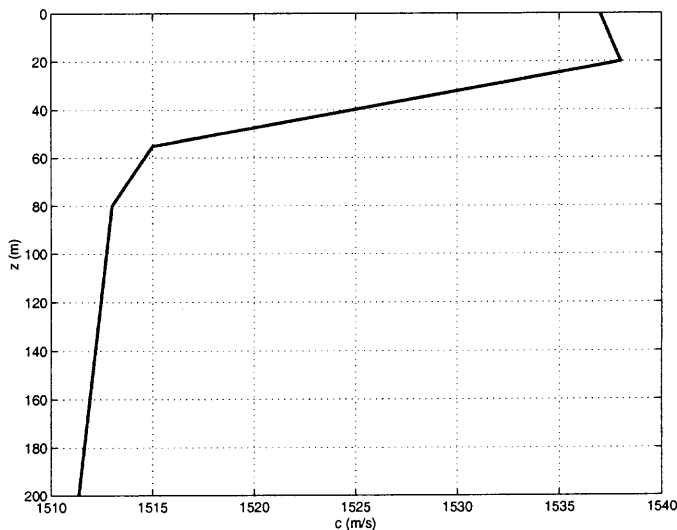


Figure 4.1 Sound speed profile for synthetic data

To perform the inversion with synthetic data, the sound speed profile is assumed initially known. The sound speed profile considered here is shown in Figure 4.1. This is a shallow water profile, simulating propagation in the Mediterranean in the summer ([19]); sound speed increases to its maximum at 20 m depth, and decreases from then on. The water depth is 200 m. The receivers are vertically separated and located between 100 and 150 m. The signal source to be localized is at a range and depth of 700 and 50 m, respectively. Figure 4.2 shows a ray trace for the chosen

environment and source and receiver parameters. The ray trace presents the different paths connecting source and receiving phones, including the paths of interest (direct, surface and bottom bounces).

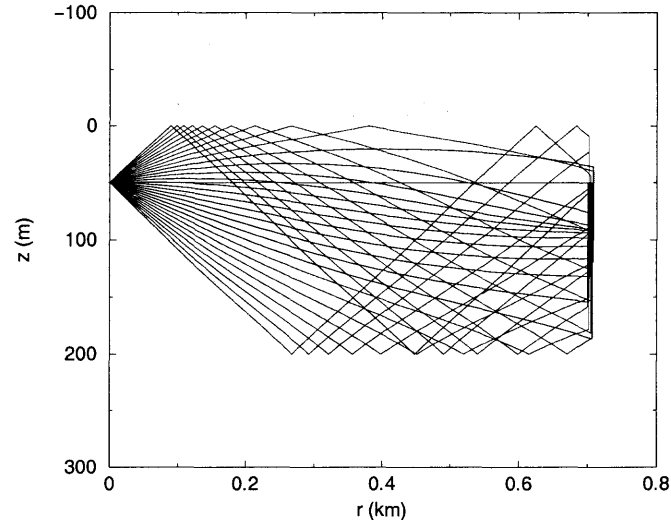


Figure 4.2 Ray trace plot of sound speed propagation.

4.2 Inversion for Source Parameters

First, it is assumed that receiver depths and ocean depth are exactly known. The least squares method is applied along with the linearization inversion scheme for the estimation of source range and depth.

4.2.1 Inversion with Arrival Times Known Exactly

In this section, localization results are studied when arrival times are measured with no error. It is initially assumed that source and receivers are synchronized leading to a known absolute time for the arrivals at the receiving phones. Table 4.1 presents location estimates obtained when arrival times of the direct path, first surface reflection, and first bottom reflection are measured and employed for the inversion. The initial conditions are 400 m and 30 m for source range and depth.

The table shows results from three different configurations involving three, five, and ten receiving phones. The results are excellent, the source location being estimated accurately only after three iterations.

number of receivers	number of iteration steps	$r(m)$	$z_s(m)$
3	3	700.00	50.00
5	3	700.01	50.00
10	3	700.00	50.00

Table 4.1 Source localization employing arrival times along three ray paths.

Table 4.2 demonstrates inversion results with five receivers for various initial conditions and different numbers of ray paths (direct; direct and surface; direct, surface, and bottom).

The selected initial conditions (IC) are:

- IC1: $r = 400\ m, z_s = 30\ m$
- IC2: $r = 800\ m, z_s = 80\ m$
- IC3: $r = 1200\ m, z_s = 125\ m$

Again, the inversion results are very good with the exact source location being recovered in each case. It can be observed that in this simulation experiment, the choice of initial conditions for the linearization scheme has no impact on the inversion results or on the iteration steps. However, with more information from different ray paths involved, the linearization scheme requires fewer iteration steps for convergence.

ray paths	number of iteration steps			inversion results	
	IC1	IC2	IC3	$r(m)$	$z_s(m)$
one path	5	5	5	700.00	50.00
two paths	3	3	3	700.00	50.00
three paths	3	3	3	700.00	50.00

Table 4.2 Source localization with different initial conditions and ray paths.

Tables 4.1 and 4.2 present results obtained assuming synchronization of source and receivers. In practice, absolute time is not always known in underwater acoustics problems and synchronization is not feasible. In such cases, the linearization process becomes more complex.

Two approaches are possible in the case of asynchronized source and receivers. The first approach is to remove the source instants from the problem by considering appropriate differences between relative travel times in the data to be inverted. The second approach is to treat the relative travel times as the data, and include the source instant as an unknown parameter to be determined in the inversion. The latter approach, also used in [13], is adopted here since it results in data with smaller uncertainties. Recall Equation 3.2:

$$d = t = \tau(r, z_s, z_r, D) + t_0,$$

where t_0 is the source instant. For the purpose of inversion, it is advantageous to scale this parameter by a representative ocean sound speed \bar{c} (1500 m/s is used in this work) leading to ([13]):

$$t = \tau(r, z_s, z_r, D) + (\bar{c}t_0)/\bar{c}. \quad (4.1)$$

By considering $\bar{c}t_0$ rather than t_0 as the unknown parameter, all parameters $(r, z_s, z_r, D, \bar{c}t_0)$ in Equation 4.1 have the same physical units, i.e., distance (scaling

parameters in this manner generally improves the numerical stability of inversion algorithms).

Table 4.3 presents localization results obtained when relative arrival times of the direct path, first surface reflection, and first bottom reflection are available. The initial conditions are 400 m and 30 m for source range and depth; the table shows results from three different configurations involving three, five, and ten receiving phones. Localization is accurate and fast; comparing Tables 4.1 and 4.3, it is observed that, in the unknown source instant case, only a few more iteration steps are required for the inversion.

number of receivers	number of iteration steps	$r(m)$	$z_s(m)$
3	5	700.00	50.00
5	5	700.00	50.00
10	4	700.00	50.00

Table 4.3 Source localization results using the linearized approach with relative times.

Table 4.4 shows the impact of initial conditions and different ray paths on the linearization scheme in the relative time case. The different initial conditions appear to have no influence on the inversion results in either absolute or relative time cases. However, when only the arrival times along the direct ray paths are taken into account, the method requires several iteration steps for convergence, and the inversion results deviate from the true source location coordinates. By taking advantage of more arrival time information along other ray paths, the exact source locations can be recovered accurately with fewer iteration steps. Comparing Tables 4.2 and 4.4 reveals that knowing the source instant can significantly improve

localization results (it is, however, more realistic in many cases to assume that only relative arrival times are available).

ray paths	number of iteration steps			inversion results	
	IC1	IC2	IC3	$r(m)$	$z_s(m)$
one path	9	9	9	634.97	55.56
two paths	5	5	5	700.00	50.00
three paths	4	4	4	700.00	50.00

Table 4.4 Source localization with five receivers using different initial conditions and ray paths and relative times.

4.2.2 Inversion with Uncertain Arrival Times

In this section, the localization results are studied when arrival times are uncertain. The uncertainty is taken into account through the addition of random noise to the arrival times. Five hundred Monte Carlo realizations are obtained in order to study the linearization method quantitatively. The initial conditions are set as: $r = 400 m$ and $z_s = 30 m$.

Figure 4.3 shows the inversion results for source range and source depth with absolute arrival times obtained along two and three paths, respectively. The temporal noise is drawn from a zero-mean Gaussian distribution with 0.5 ms standard deviation.

Figures 4.3 (a) and (b) show the histograms of the inversion results for the two path case; Figures 4.3 (c) and (d) present the histograms of the results for the three path case. The histograms show that the mean values of the simulation results match well with the exact source location with very small standard deviations (std). It is also noticed that the error in the inversion results is of the same order for both two and three path inversion. The average number of iteration steps is 6, indicating that the linearization method is efficient.

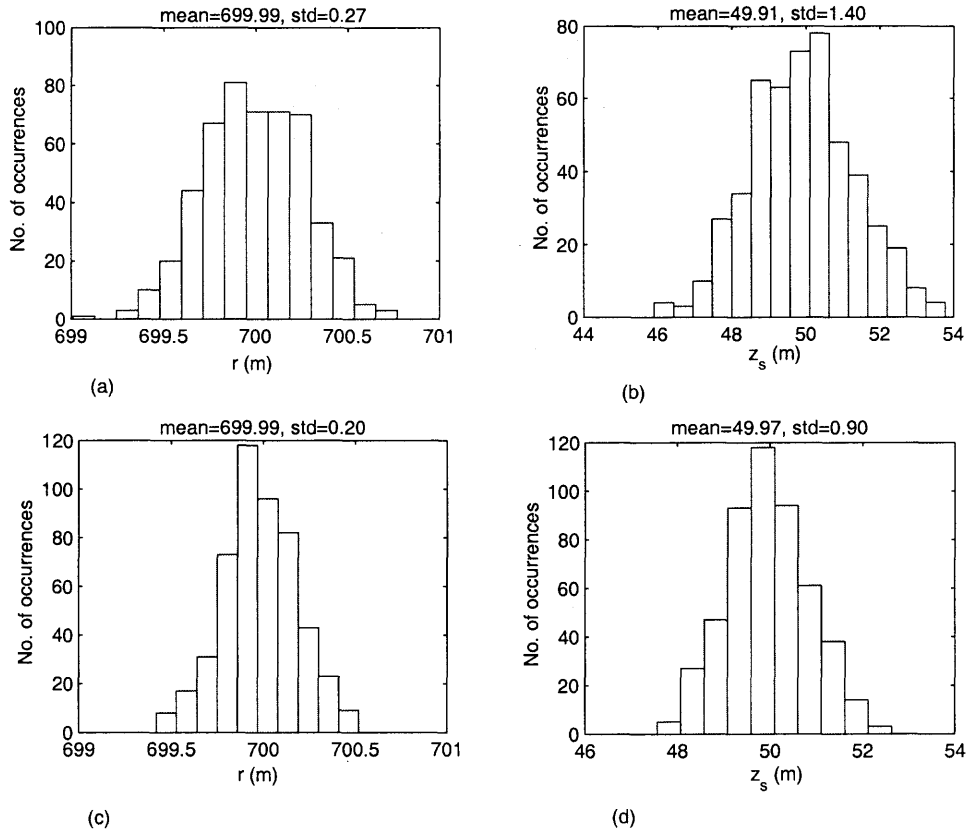


Figure 4.3 Histograms calculated from Monte Carlo simulations for source localization using absolute arrival times: (a) source range in two path case; (b) source depth in two path case; (c) source range in three path case; (d) source depth in three path case.

Meanwhile, as expected, the histograms of Figures 4.3 (a) and (b) have a wider spread than those of Figures 4.3 (c) and (d). This indicates that the linearization method yields better inversion results when it explores information from more ray paths (recall that bottom depth is assumed to be known).

Table 4.5 shows the inversion results with different time uncertainties (that is, standard deviation of the Gaussian distribution for the time errors) using arrival times for five receivers and three paths. The mean values for source range and depth are very close to the exact solution even for the larger values of time uncertainty. The standard deviations for the estimation of both parameters are increasing almost linearly with respect to time uncertainty.

time uncertainty	mean r	std r	mean z_s	std z_s
0.5 ms	699.98	0.20	49.97	0.89
1 ms	699.97	0.42	50.07	1.79
2 ms	700.05	0.91	49.82	3.67
4 ms	700.09	1.81	49.67	7.13

Table 4.5 Source localization results with different arrival time uncertainties.

The Monte Carlo results for the relative arrival time case are shown in Figure 4.4. Figures 4.4 (a) and (b) shows the histograms of the inversion results for source range and source depth in the two path case; Figure 4.4 (c) and (d) present the histograms in the three path case. The histograms show that the mean values are very close to the exact source locations in the three path case. Again, as anticipated, the histograms in the two path case have a larger spread than in the three path case leading to a larger error in the estimation. In fact, the standard deviations for both parameters in the two path case is about 6 times larger than in the three path case. It is also noticed that when only relative arrival times are available, the inversion errors for source range are much bigger than those for source depth.

Figure 4.5 presents scatter plots of source range and source depth from the Monte Carlo inversion. Figure 4.5 (a) shows a scatter plot of the inversion results for the two path case and Figure 4.5 (b) presents a scatter plot for the three path case. Comparing Figures 4.5 (a) and 4.5 (b) demonstrates in a different fashion that the inversion results are superior in the three path case compared to those in the two path case, showing the reduction of the spread in range estimation.

The scatter plot of Figure 4.5 (a) shows nicely the linear relationship between source range and depth which is implied by the linearizing nature of this work. This

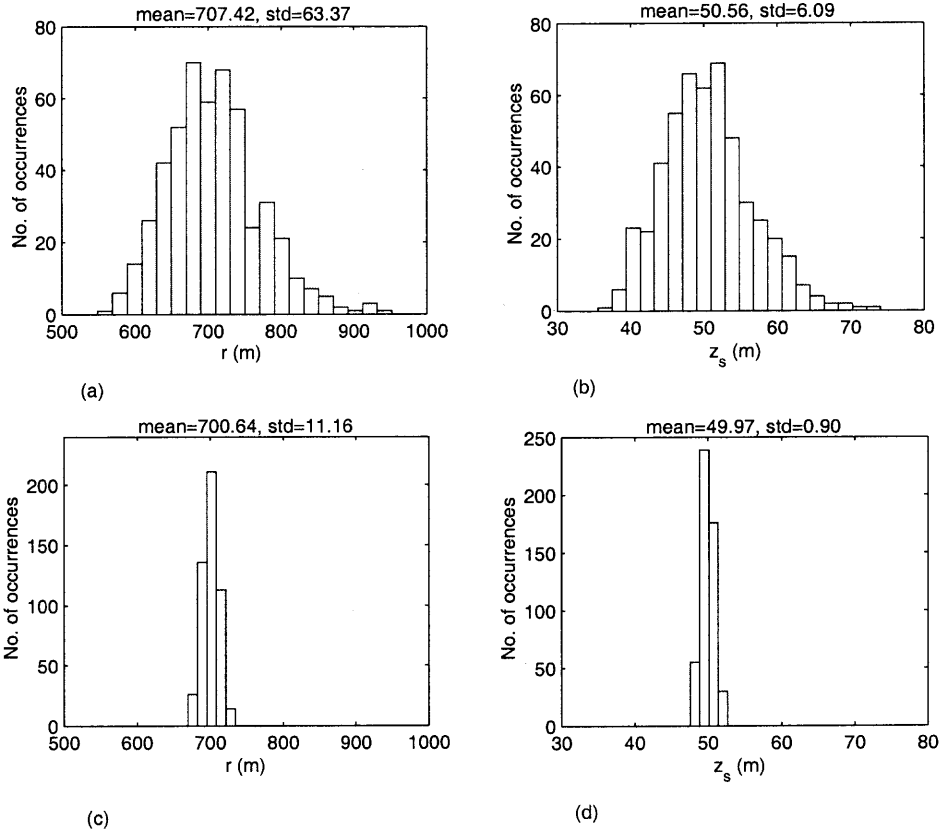


Figure 4.4 Histograms calculated from Monte Carlo simulations for source localization using relative arrival times: (a) source range in two path case; (b) source depth in two path case; (c) source range in three path case; (d) source depth in three path case.

relationship can be also illustrated using the following simple analysis. Assume that t_d is the travel time along the direct path from source to receiver; and t_s is the travel time along the first surface bounce path. These two travel times can be expressed as:

$$t_d = \sqrt{r^2 + (z_r - z_s)^2}/c$$

$$t_s = \sqrt{r^2 + (z_r + z_s)^2}/c$$

where r is the source range, z_s and z_r are the source and receiver depths, and c is the sound speed. Therefore,

$$\begin{aligned} \Delta t &= t_s - t_d \\ &= \frac{\sqrt{r^2 + (z_r + z_s)^2} - \sqrt{r^2 + (z_r - z_s)^2}}{c} \end{aligned}$$

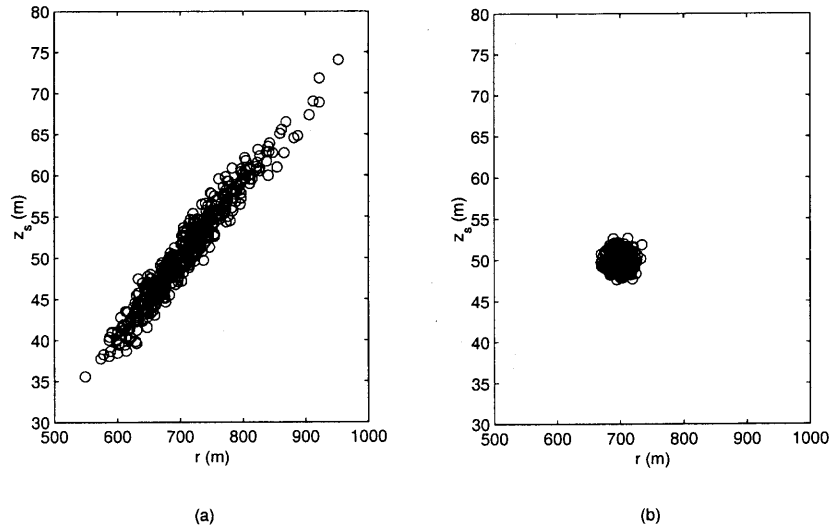


Figure 4.5 Monte Carlo simulations for source localization using relative arrival times: (a) scatter plots of depth vs. range in two path case; (b) scatter plots of depth vs. range in three path case.

$$= \frac{4z_r z_s}{c[\sqrt{r^2 + (z_r + z_s)^2} + \sqrt{r^2 + (z_r - z_s)^2}]}$$

For fixed z_r , it can be concluded that

$$\Delta t \sim \frac{z_s}{r},$$

which explains the linear pattern in the inversion results. This relationship also reminds us that for a large range r , the time difference between direct path and surface reflection becomes very small, whereas it increases as the source is positioned in deeper water.

time uncertainty	mean r	std r	mean z_s	std z_s
0.5 ms	700.64	11.16	49.97	0.90
1 ms	696.55	22.07	49.93	1.81
2 ms	705.96	45.39	50.17	3.72
4 ms	687.45	88.37	50.21	7.55

Table 4.6 Source localization results with different arrival time uncertainties using relative arrival times.

Table 4.6 shows inversion results with different time uncertainties, using arrival times for three paths. As time uncertainty increases, the mean value for source range starts to deviate from the true range. However, the mean value for source depth is still very close to the true depth. The standard deviation for source range is about 10 times larger than that for source depth. This indicates again that for the relative arrival time case the localization error is dominated by the source range. This is expected since ray travel times depend on ray travel distance. In the case when $r \gg z_s$ and $r \gg z_r$, the variations in source range contribute much more to variations in travel time than other parameters.

Comparing absolute and relative time cases (Table 4.5 and Table 4.6) shows that the inversion results for source depth in both absolute and relative arrival time cases have similar errors. However, in the relative time case, the standard deviation for source range is fifty times larger than that in the absolute time case. In general, however, the linearization inversion results are still very good in the relative time case, with an average of 10 iteration steps required for convergence. In summary, good localization results are obtained with small computational requirements.

4.3 Inversion for Source Parameters in an Uncertain Environment

In the previous section, the inversion results were presented for the case when the ocean bottom depth, receiver hydrophone depths, and sound speed profile are all known exactly. In practice, it is often difficult to obtain accurate information for some of these parameters. In this section, parameter uncertainties are considered in the localization process.

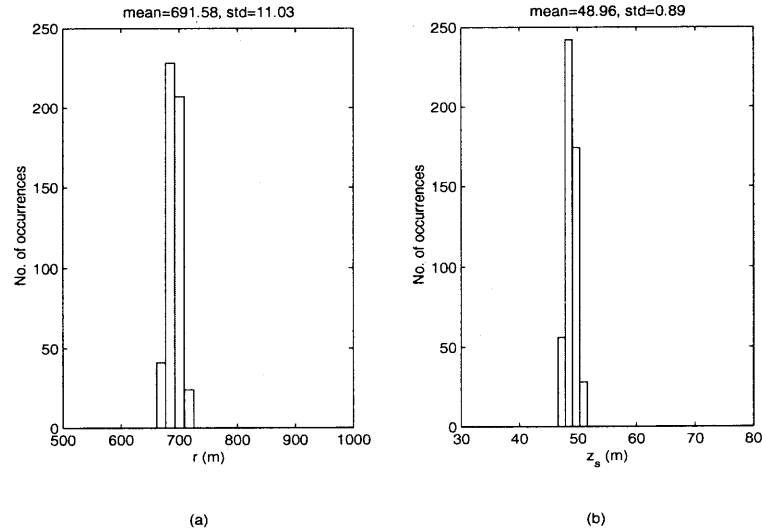


Figure 4.6 Monte Carlo simulations for source coordinate inversion using relative arrival times and introducing an error in one receiver depth: (a) histogram of source range; (b) histogram of source depth.

4.3.1 Inversion Sensitivity to Receiver Depth

The arrival times along three paths are used (including the first bottom bounce path) to study the uncertainty in receiver depths. Figure 4.6 shows the Monte Carlo inversion results with a 5 m error for the top receiver depth (the exact top receiver depth is 110 m and the assumed receiver depth is 115 m).

Comparing Figures 4.6 (a) and (b) to Figures 4.4 (c) and (d) shows that the mean values of source range and depth are both off from the true values when there is error in the receiver depth information. The source range has an 8 m error and the source depth has an error of approximately 1 m. However, the standard deviations for source depth and source range are almost the same whether the receiver depth is accurately known or not (it appears as if the distributions of the estimates have been shifted because of the receiver depth error).

4.3.2 Inversion Sensitivity to Ocean Bottom Depth

To study the uncertainty with respect to the ocean bottom depth, the arrival times along three paths are employed including the first bottom reflection path. Figure 4.7 shows the inversion results with a 5 m error for bottom depth (the exact bottom depth is 200 m and the assumed bottom depth is 205 m).

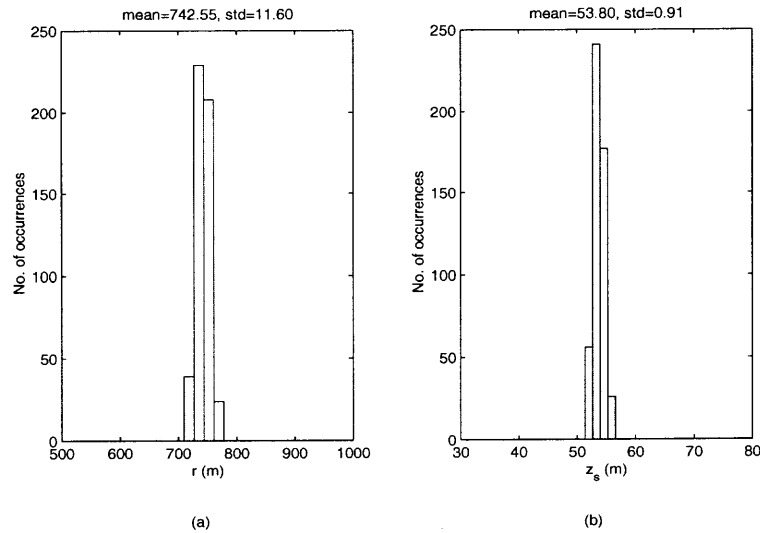


Figure 4.7 Monte Carlo simulations for source coordinates inversion using relative arrival times and introducing an error in bottom depth: (a) histogram of source range; (b) histogram of source depth.

As in the receiver depth mismatch case, comparing Figures 4.7 (a) and (b) to Figures 4.4 (c) and (d) shows that the mean values of source range and depth are both off from the true values when there is error in the bottom depth information. The source range has a 42 m error and the source depth has an error of approximately 4 m. However, the standard deviations for source depth and source range are still almost the same whether the bottom depth is accurately known or not. The observation of a range shift with a bottom depth error has been extensively discussed in [4, 15, 27].

In order to reduce localization errors due to lack of accurate information on bottom and receiver depth, these parameters are included as unknowns in the inversion process. The process is started by studying the problem of inversion for the depth of the water column.

4.3.3 Ocean Bottom Depth Inversion

In this section, the ocean bottom depth is included as an unknown parameter in the linearization inversion process. First, the least squares method is employed for the solution of the linear system. Arrival times along three paths including the first bottom reflection are taken into account. The initial conditions are: $r = 400$ m, $z_s = 30$ m, $D = 180$ m. Figure 4.8 shows the simulation results using absolute arrival times, with zero mean and 0.5 ms standard deviation for temporal uncertainty. Figures 4.8 (a), (b) and (c) show the histograms for source range, source depth and bottom depth, respectively.

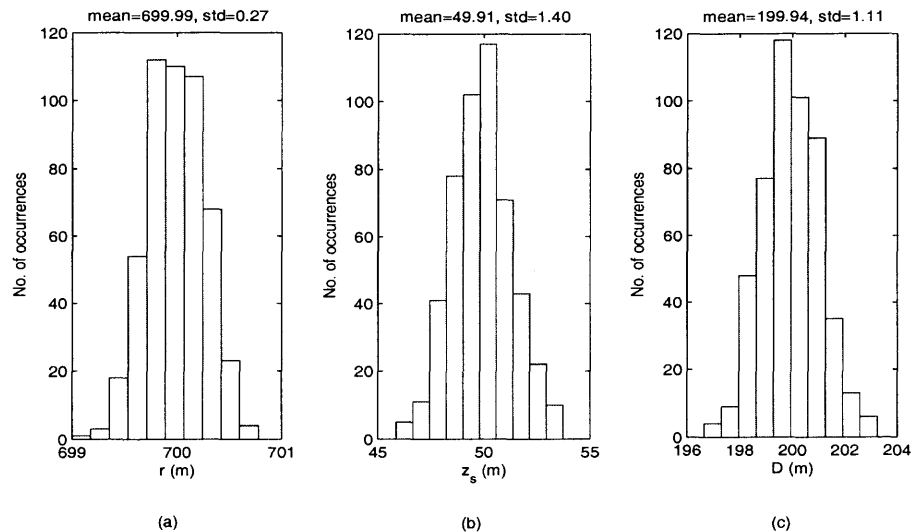


Figure 4.8 Monte Carlo simulations for source and bottom parameters inversion using absolute arrival times and three paths: (a) histogram of source range (b) histogram of source depth (c) histogram of bottom depth

Comparing Figure 4.8 to Figure 4.3, it can be observed that, with unknown bottom depth, the inversion results for source location still match well with the exact parameter values in the absolute time case.

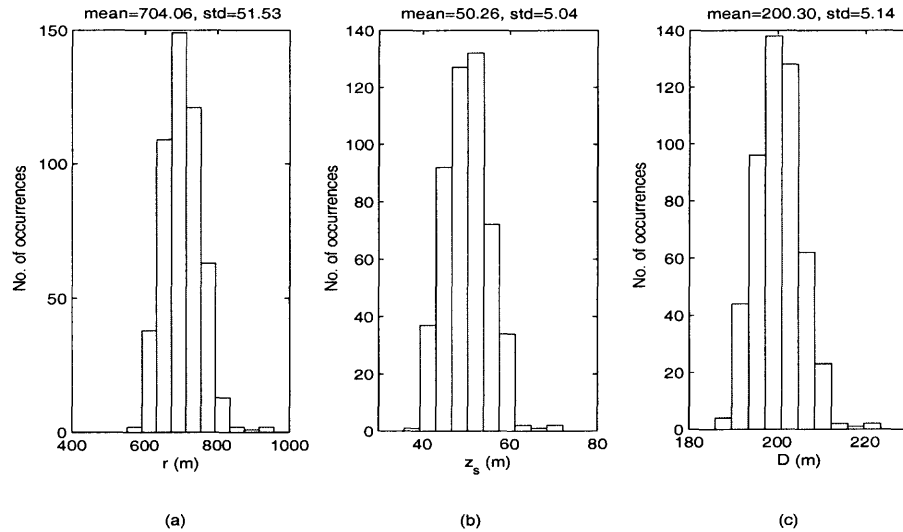


Figure 4.9 Histograms calculated from Monte Carlo simulations for source and bottom parameters inversion using relative arrival times and three paths: (a) histogram of source range (b) histogram of source depth (c) histogram of bottom depth.

Figure 4.9 shows the simulation results using relative arrival times. Comparing Figure 4.9 to Figure 4.4 shows that, when only relative arrival times are available, source localization results are degraded when bottom depth is added as an unknown. This observation is mainly based on the increased values of standard deviation for the uncertain bottom depth case. The mean values and standard deviations for source range and depth are comparable to those of the two path case when the bottom reflection path is not included. However, source location estimates in the mean value sense are satisfactory.

When a priori information on the bottom depth is available, regularization instead of simple least squares can be employed in the linearization process. Figure 4.10 shows the simulation results in the relative arrival time case assuming that bottom depth is approximately known with an uncertainty of 5 m. The standard deviation in the temporal uncertainty is still 0.5 ms.

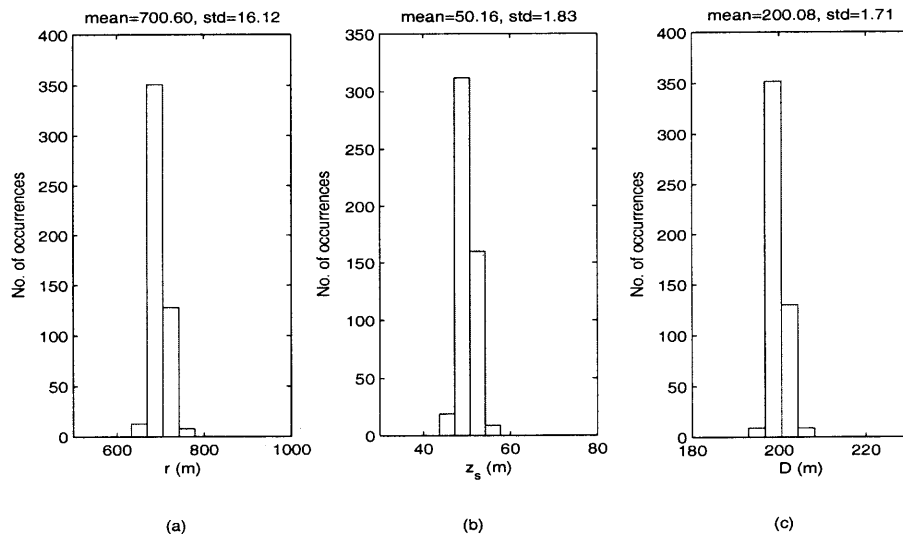


Figure 4.10 Histograms calculated from Monte Carlo simulations for source and bottom parameters inversion using regularization and relative arrival times: (a) histogram of source range (b) histogram of source depth (c) histogram of bottom depth.

Comparing Figure 4.10 to Figures 4.9 and 4.7 shows that when the bottom depth is inaccurately known, better results can be attained by introducing the regularization method in the inversion process. The mean values of source range and source depth (and also the bottom depth) agree closely with the true values of the parameters. When bottom depth is inverted for, the standard deviations in the estimation of the unknown parameters are substantially reduced when regularization is introduced.

Comparing Figure 4.10 to Figure 4.4 shows that the inversion results using the regularization method and three paths are much better than those from the two-path inversion. The standard deviations of the source range and source depth are only slightly larger than those of the three path case when the bottom depth is known.

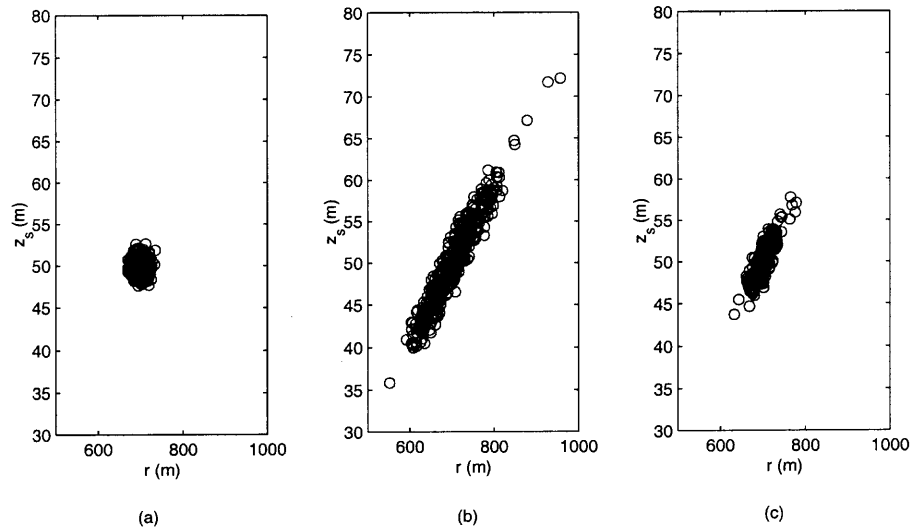


Figure 4.11 Results from Monte Carlo simulations for source and receiver parameters inversion using relative arrival times and three ray paths with known receiver depth: (a) scatter plot using the least squares method with bottom depth known exactly; (b) scatter plot using the least squares method with bottom depth unknown; (c) scatter plot using the regularization method with bottom depth unknown.

Figure 4.11 presents the scatter plots (source range vs. source depth) from different inversion schemes. A comparison of the scatter plots shows once again the reduction in the spread (error) in source location estimates when the regularization method is employed exploiting prior information on the unknown bottom depth. Naturally, the smallest spread is observed when the bottom depth is perfectly known.

Figure 4.12 presents the scatter plots of source range vs. bottom depth. Both scatter plots show linear patterns with positive slope. This linear trend has been frequently discussed in the underwater inversion literature; it is the source of

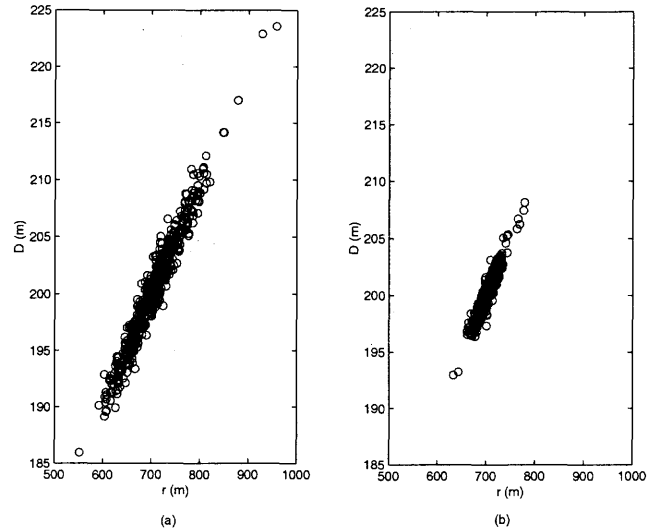


Figure 4.12 Monte Carlo simulations for source range and bottom depth inversion using relative arrival times and three ray paths: (a) scatter plots using least squares method; (b) scatter plots using regularization method.

the range shift previously discussed when there is an error in the bottom depth assumption.

4.4 Including Receiver Depths in the Inversion Process

In the previous subsections, the sensitivity of the inversion results to receiver depth and bottom depth were discussed. In the case of uncertain bottom depth, linearized inversion was employed with least squares and regularization inverting for both source location and water column depth. However, when the receiver depths are uncertain and are treated as unknown, the linearization inversion using least squares generally gives unstable results ([13]). In this section, inversion using regularization is performed for the case of uncertain receiver depths.

Initially, the top receiver depth is approximately known within 5 m and the bottom depth is assumed to be known exactly.

Figure 4.13 shows the simulation results in the relative arrival time and three path case (the standard deviation of arrival time error is 0.5 ms).

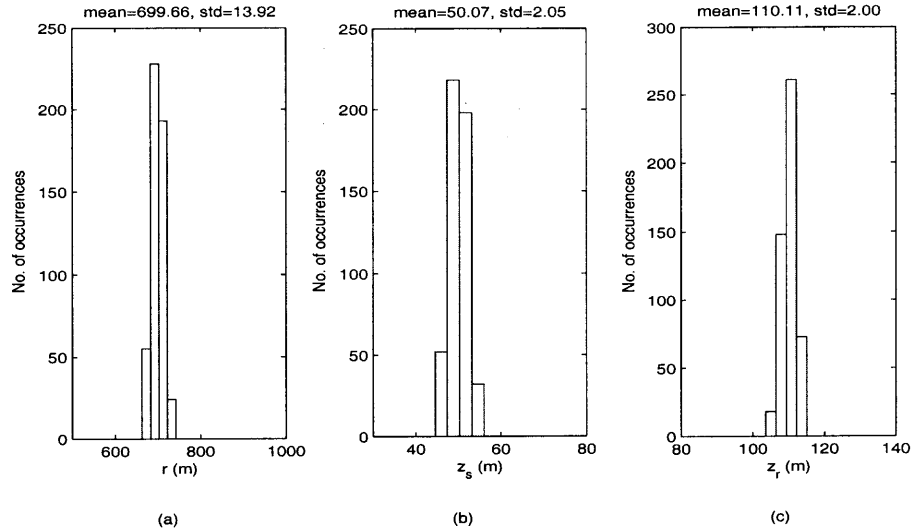


Figure 4.13 Monte Carlo simulations for source and receiver parameter inversion using regularization and relative arrival times: (a) histogram of source range (b) histogram of source depth (c) histogram of top receiver depth.

Comparing Figure 4.13 to Figures 4.4 (c) and (d) shows that the inversion results using regularization and one uncertain receiver depth are still good, with standard deviations in the estimation slightly increased because of the receiver depth uncertainty.

Finally, inversion results using regularization are obtained when **all** receiver locations and bottom depth are uncertain. Figure 4.14 shows the histograms calculated from Monte Carlo simulation results. These results incorporate all uncertainty considered so far and represent estimates that would be obtained in practice when many parameters are not accurately known.

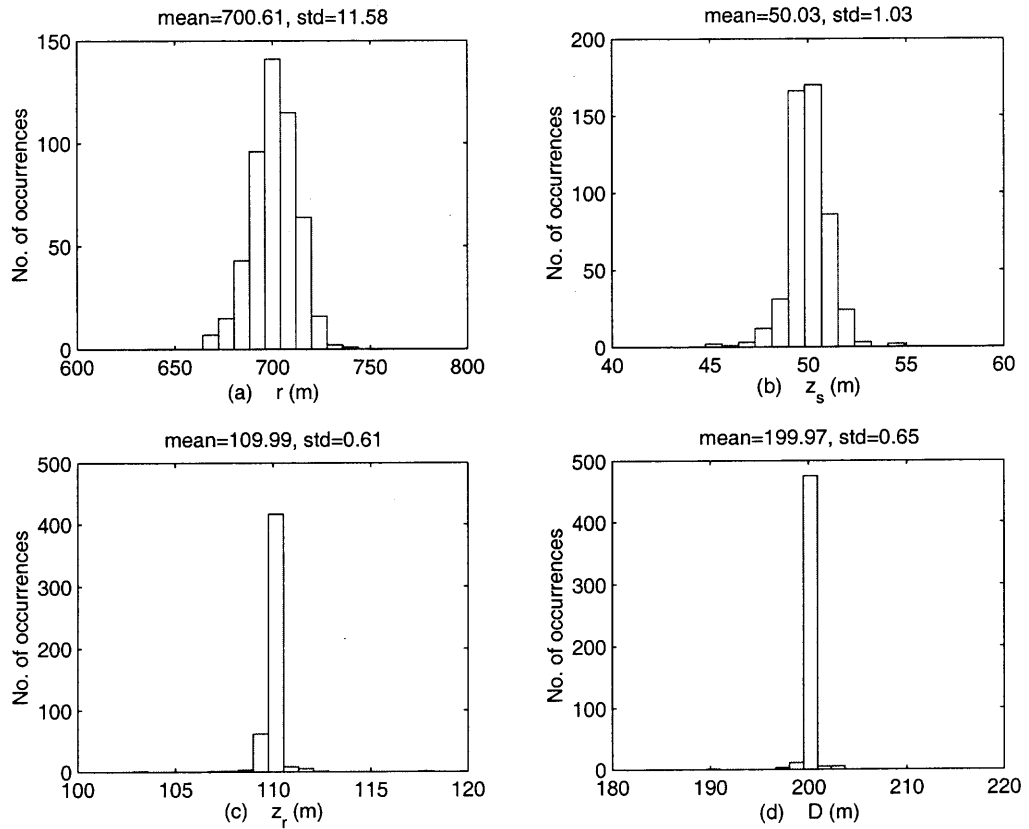


Figure 4.14 Monte Carlo simulations for source and receiver location and bottom depth inversion through regularization with relative arrival times and three ray paths: (a) histogram of source range (b) histogram of source depth (c) histogram of receiver depth (d) histogram of bottom depth.

CHAPTER 5

INVERSION FOR SOUND SPEED PROFILE

In this chapter the impact of sound speed knowledge on source localization is investigated. First, localization is performed assuming an isovelocity sound speed profile. Then, the sensitivity of the inversion process is studied with respect to other sound speed errors. Finally, inversion for sound speed is implemented using empirical orthogonal functions.

5.1 Localization under the Assumption of an Isovelocity Sound Speed Profile

Table 5.1 presents source localization results (three path case) when the sound speed profile is assumed to be a depth independent constant (mean of the sound speed profile in Figure 4.1). The table shows that when the sound speed profile is approximated with its mean value in the water column, the inversion results are degraded in both absolute arrival time and relative arrival time cases.

arrival time case	r (m)	z_s (m)
Absolute time	702.25	39.19
Relative time	732.85	37.33

Table 5.1 Source localization results using a constant sound speed profile in the three path case.

The approximation of the refracted ray paths using straight-line rays (due to the constant sound speed profile) generates significant errors in arrival times and leads to poor source localization results. This indicates the importance of the knowledge of the true sound speed in the source localization process. The results of Table 5.1 were

calculated with no uncertainty in the arrival times. Localization is further degraded, when temporal uncertainty is considered.

5.2 Sensitivity of Source Localization to Sound Speed Uncertainty

The purpose of this section is to study the sensitivity of the linearization inversion method to errors in sound speed profile assumptions using two approaches (see Figure 5.1):

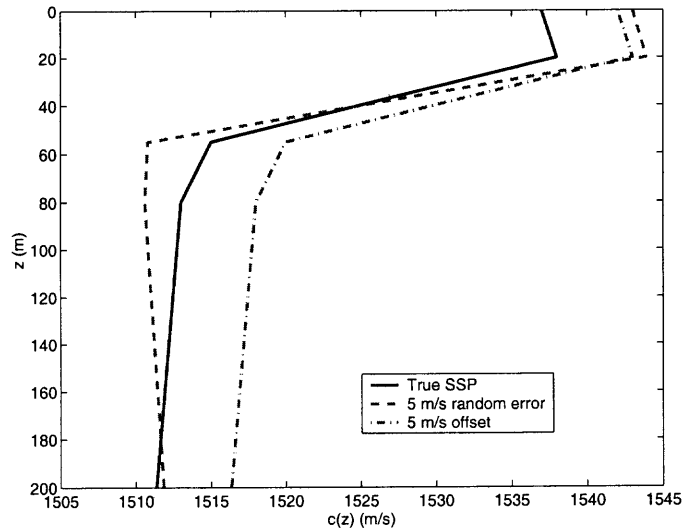


Figure 5.1 Sound-speed profile mismatch

1. a depth-independent error of 5 m/s is added to each sound speed in the water column;
2. a normally distributed error with zero mean and 5 m/s deviation is added to the sound speed.

Table 5.2 shows the localization results from both approaches in the relative arrival time case. From the results it can be observed that results are still close to

SSP	r	z_s
offset	696.54	49.37
random error	652.02	52.35

Table 5.2 Source localization results under sound speed uncertainty in the three path case with relative arrival times known exactly.

the true location values in the case of the sound speed offset; however, in the random error case, the inversion generates a localization error, especially for the source range.

5.3 Sound Speed Profile Inversion

5.3.1 EOF Model

Sound speed estimation is one of the key goals in ocean acoustic tomography ([4, 14, 15, 28, 29, 30]). In this work, inversion for sound speed is approached using empirical orthogonal functions (EOFs) [31]. The true sound speed profile \mathbf{c} is modeled as:

$$\mathbf{c}(z) = \mathbf{c}_m(z) + \mu \mathbf{v}_1(z), \quad (5.1)$$

where $\mathbf{c}_m(z)$ is a mean sound speed profile, $\mathbf{v}_1(z)$ is the eigenvector (corresponding to the largest eigenvalue) of the “excess” sound speed covariance matrix constructed from different sound speed profile measurements and $\mathbf{c}_m(z)$, and μ is the unknown multiplicative coefficient of the perturbation that needs to be estimated. The presence of $\mathbf{v}_1(z)$ in the EOF model is due to the fact that larger eigenvalues are more statistically significant than smaller ones. Smaller eigenvalues are more subject to noise and their associated eigenvectors are more related to sampling errors than to actual physical phenomena.

Assuming that there are N measured sound speed profiles $[\mathbf{c}_1, \mathbf{c}_2, \dots, \mathbf{c}_N]$, \mathbf{c}_m is given by:

$$\mathbf{c}_m = \frac{\sum_{i=1}^N \mathbf{c}_i}{N}. \quad (5.2)$$

The i th vector of the excess sound speed matrix \mathbf{E} is then defined as:

$$\mathbf{E}_i = \mathbf{c}_i - \mathbf{c}_m. \quad (5.3)$$

The excess sound speed covariance matrix \mathbf{V} can be obtained by:

$$\mathbf{V} = \mathbf{E}\mathbf{E}^T/N, \quad (5.4)$$

from which eigenvector \mathbf{v}_1 is determined.

In order to perform the inversion of the sound speed coefficient μ , time derivatives with respect to μ are required. The derivation is presented in Appendix B. In the following sections, the sound speed coefficient inversion is studied with simulated data.

5.3.2 Inversion without Temporal Noise

To apply the EOF model for the sound speed coefficient inversion, five estimated sound speed profiles are simulated and considered as “collected” data as shown in Figure 5.2.

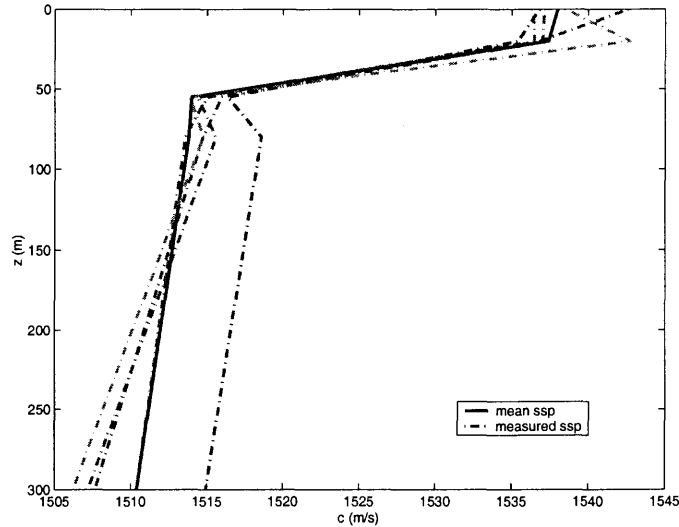


Figure 5.2 Measured and mean sound speed profile data.

The mean sound speed $\mathbf{c}_m(z)$ and the eigenvector $\mathbf{v}_1(z)$ are then calculated and presented in Table 5.3.

z (m)	$c_m(z)$	$v_1(z)$
0	1538.0	-0.5
20	1537.4	0.3
55	1514.0	0.5
80	1513.8	-0.4
300	1510.4	-0.2

Table 5.3 Sound speed profile data for EOF model

The true sound speed profile follows Figure 4.1, corresponding to $\mu=2$. To study the inversion in more detail, three different sets of initial conditions are chosen:

- IC1: $r = 400$ m, $z_s = 30$ m
- IC2: $r = 800$ m, $z_s = 80$ m
- IC3: $r = 1200$ m, $z_s = 125$ m

The inversion results from the linearization method using least squares showed that, when arrival times (either absolute arrival times or relative arrival times) are assumed known, the estimated results agree well with the true data under any group of initial conditions (IC1-IC3).

5.3.3 Inversion with Uncertain Arrival Times

Next localization results are obtained using least squares with arrival time uncertainty, which is again taken into account through the addition of random noise to the arrival times. The temporal standard deviation is 0.5 ms.

Figure 5.3 shows the inversion results from 500 Monte Carlo runs with absolute arrival times obtained along three paths: Figures 5.3 (a), (b) and (c) show the histograms of the inversion for source range, source depth, and sound

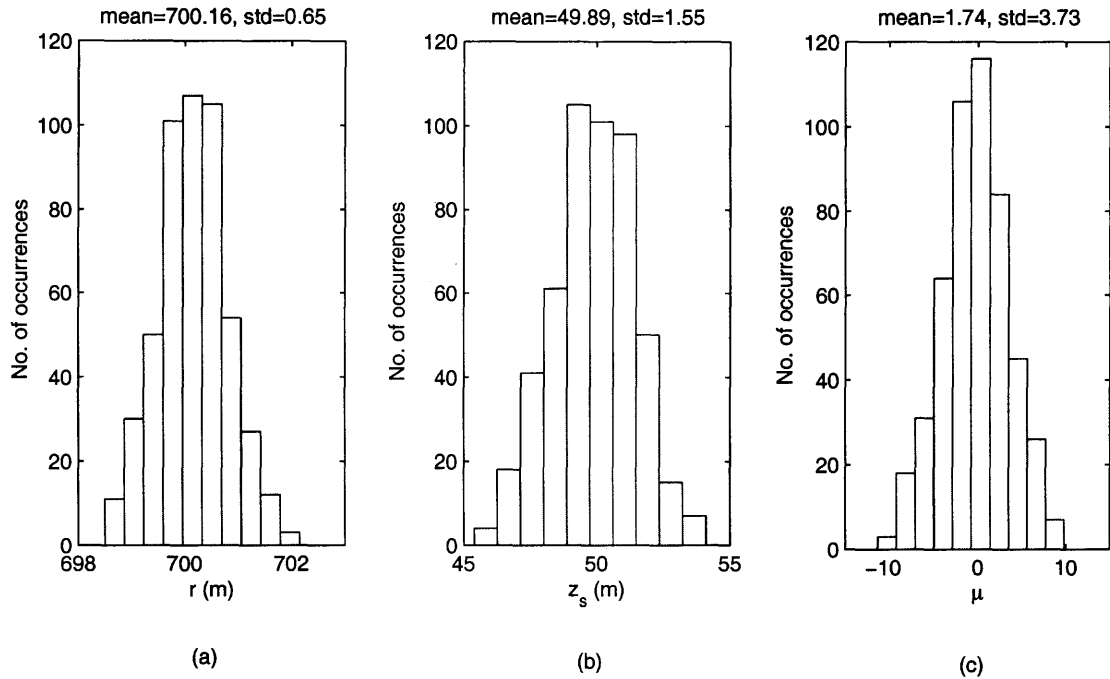


Figure 5.3 Histograms calculated from Monte Carlo simulations for source localization and sound speed coefficient estimation using three ray paths and absolute arrival times: (a) histogram of source range (b) histogram of source depth (c) histogram of sound speed coefficient.

speed coefficient, respectively. The mean values for the estimated parameters are all very close to the true parameter values with small standard deviations.

The sensitivity of the inversion to various initial conditions was also studied in this case. It turns out that the same inversion results are produced from all initial condition sets.

Figure 5.4 shows the inversion results with relative arrival times obtained along three paths, with Figures 5.4 (a), (b) and (c) showing the histograms of the inversion for source range, source depth, and sound speed coefficient. As expected, the inversion results with uncertain relative arrival times have larger errors than those with uncertain absolute arrival times. Nonetheless, localization gives range and depth estimates close to their true values. Also the sound speed coefficient μ

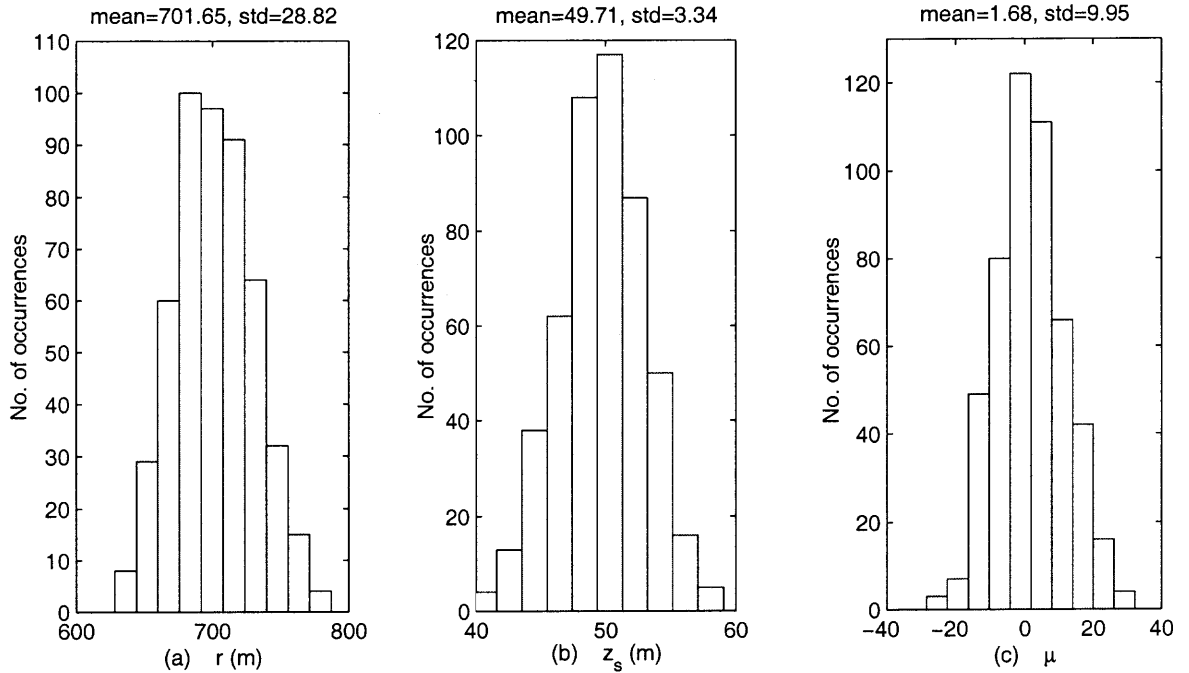


Figure 5.4 Histograms calculated from Monte Carlo simulations for source localization and sound speed coefficient estimation using three ray paths and relative arrival times: (a) histogram of source range (b) histogram of source depth (c) histogram of sound speed coefficient.

is recovered successfully, although, because of the short ranges considered here, the sensitivity to μ is not very pronounced and the standard deviation is not negligible.

It has been shown in this chapter as well as in Chapter 4 that the source localization using the proposed linearization method can be achieved successfully under various circumstances.

All uncertainties considered so far are summarized here and include in the localization process bottom depth, receiver locations, and sound speed coefficient as unknowns. Regularization is employed for the inversion.

Figure 5.5 presents the histograms of estimation results for the following parameters: source range, source depth, bottom depth, receiver locations, and

sound speed coefficient (all receiver locations are here uncertain). The uncertainties for each receiver depth and bottom depth are 5 m. The uncertainty for μ is 10. The regularization method is applied for inversion. The arrival time noise is again simulated using a zero mean Gaussian distribution with 0.5 ms standard deviation. Range and depth are recovered successfully. The other unknown parameters are also accurately estimated. Comparing Figure 5.5 to Figure 5.4, it is particularly noticeable that the standard deviation in the sound speed coefficient drops significantly, when regularization is employed instead of least squares.

Figures 5.6 and 5.7 presents the histograms of inversion results when the temporal noise standard deviation for the arrival times is increased to 1 ms and 2 ms, respectively. As expected, standard deviations in the estimation increase with increasing noise level; the mean values are hardly affected.

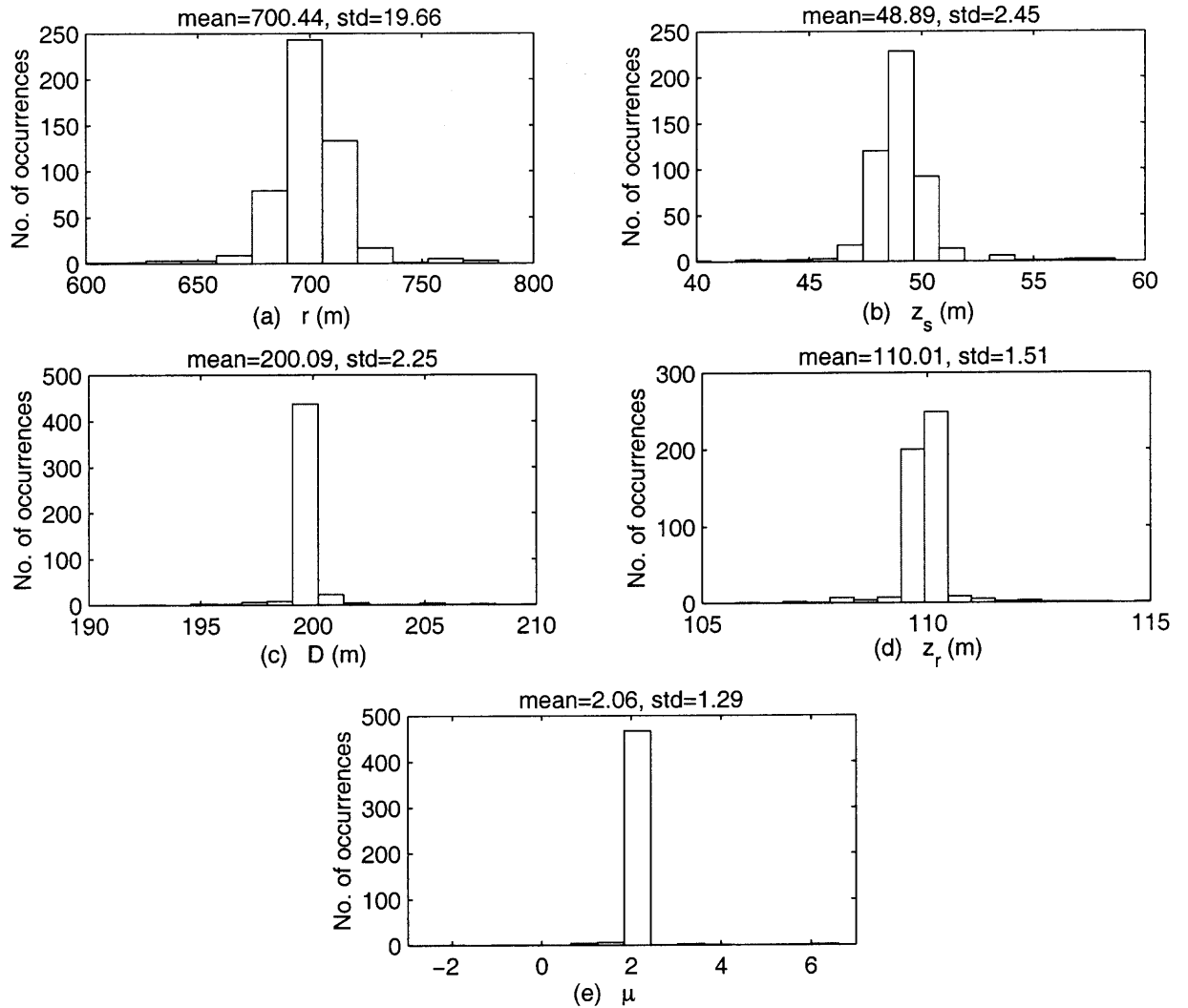


Figure 5.5 Histograms from Monte Carlo simulations for source localization using regularization with three ray paths and relative arrival times (0.5 ms temporal noise): (a) histogram of source range (b) histogram of source depth (c) histogram of bottom depth (d) histogram of top receiver depth (e) histogram of sound speed coefficient.

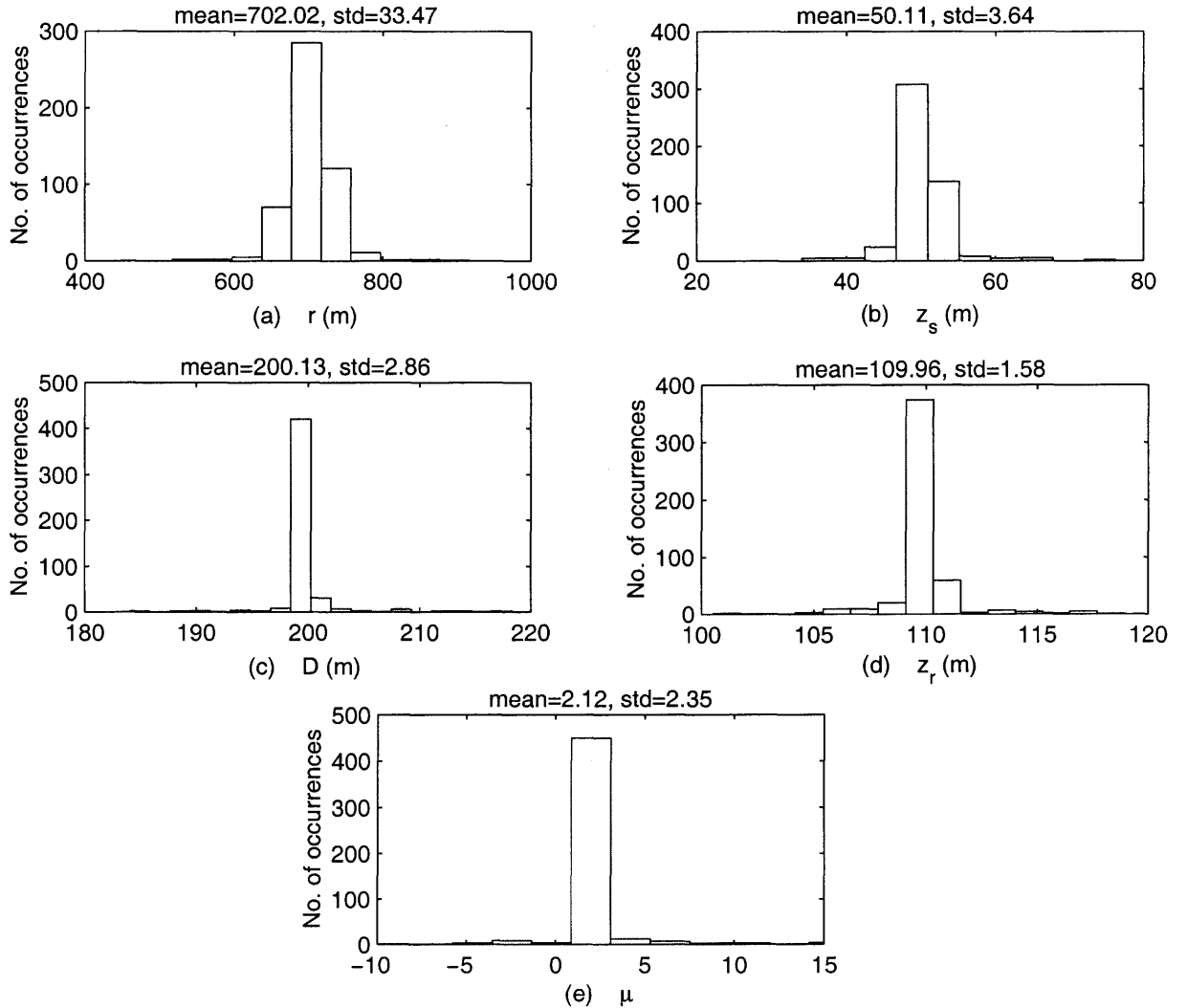


Figure 5.6 Histograms from Monte Carlo simulations for source localization using regularization with three ray paths and relative arrival times (1 ms temporal noise): (a) histogram of source range (b) histogram of source depth (c) histogram of bottom depth (d) histogram of top receiver depth (e) histogram of sound speed coefficient.

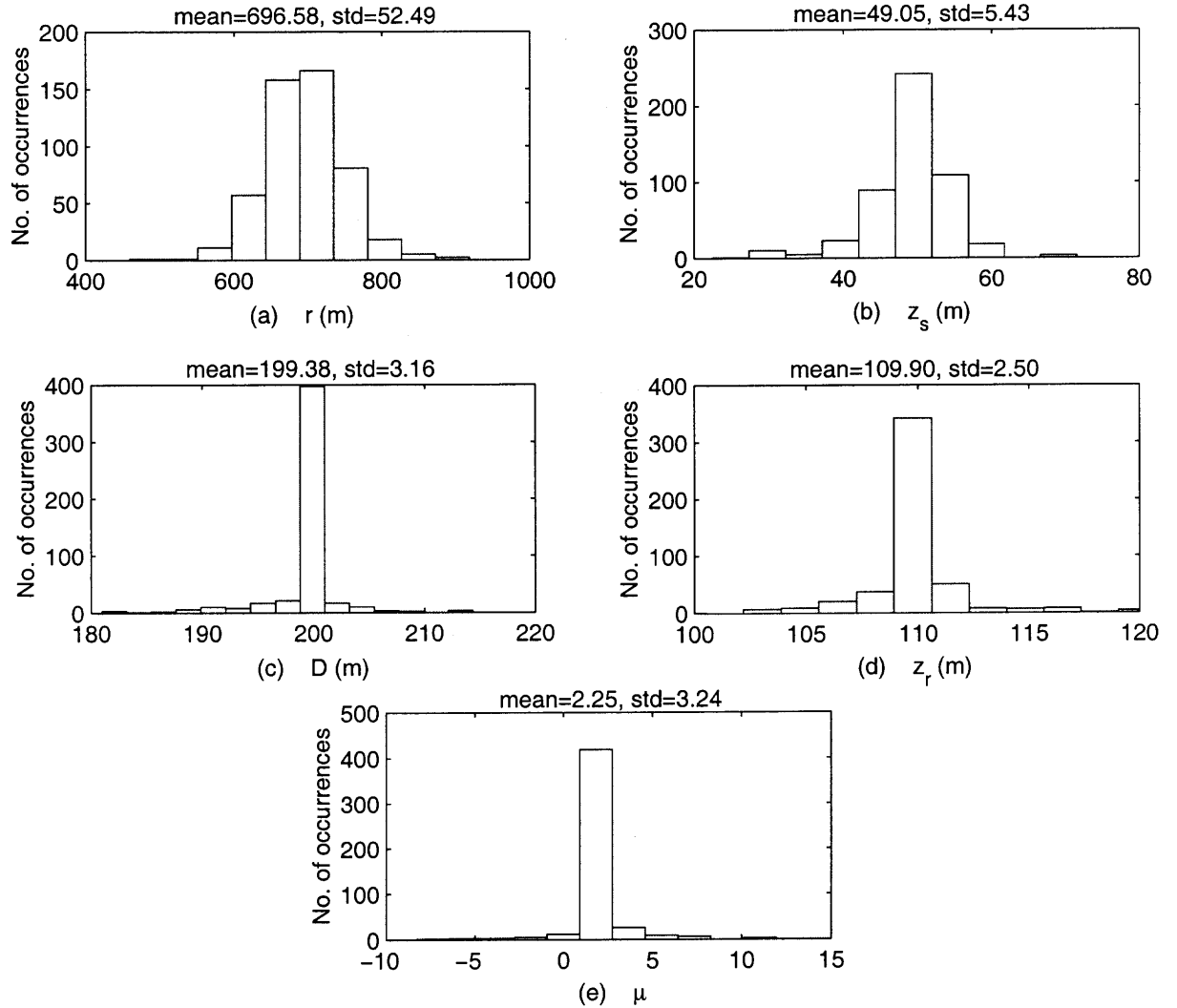


Figure 5.7 Histograms from Monte Carlo simulations for source localization using regularization with three ray paths and relative arrival times (2 ms temporal noise): (a) histogram of source range (b) histogram of source depth (c) histogram of bottom depth (d) histogram of top receiver depth (e) histogram of sound speed coefficient.

CHAPTER 6

INVERSION WITH REAL DATA

In this chapter, linearized inversion is applied to real data from the Haro Strait experiment. Both least squares and regularization are employed in the inversion process for comparison and discussion.

6.1 Haro Strait Experiment

This experiment was carried out in June of 1996 at Haro Strait, on the east coast of South Vancouver Island. The experiment took advantage of the MIT/WHOI system of vertical line arrays (VLAs) and data acquisition system. The underwater sound speed profile, measured using a velocimeter, was found to be independent of depth with a value of approximately 1482.5 m/s.

The surveyed area was range dependent with respect to bathymetry, with the depth ranging roughly between 150 and 200 m. Each VLA consisted of 16 hydrophones with a vertical spacing of approximately 6 m between phones, and a total aperture of 100 m (Figure 6.1). Acoustic data were recorded at a sampling rate of 1750 Hz.

Sound signals were provided by standard household light bulbs that were deployed using a fishing line apparatus. Light bulb shots were triggered at depths of 30-70 m. The signals generated by the light bulb contain broadband information (100-800 Hz). Figure 6.2 shows the locations of three VLAs (NW, SW, NE) and the light bulbs deployed in the Haro Strait.

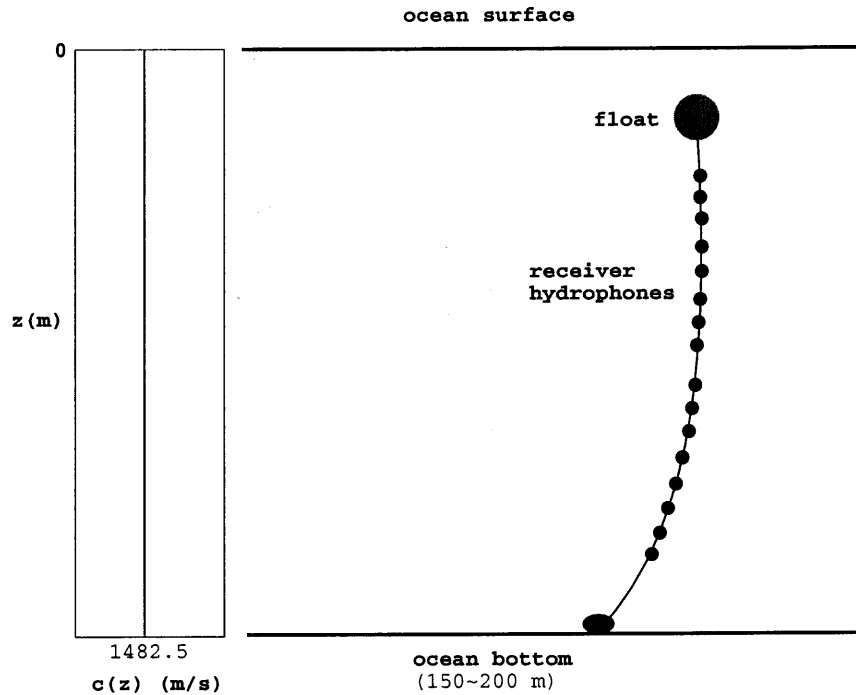


Figure 6.1 A sketch of the Haro Strait experiment.

6.2 Localization Results

In this section, the linearization inversion approach is applied to acoustic data recorded at the NE, SW, and NW array.

6.2.1 Reference Data

The source and VLA position were estimated during the experiment. Approximate location information was made available to us along with the data. The accuracy of these estimates was about ± 25 m in the range, and ± 3 m for the source and hydrophone depths [32]. Coordinates made available to us were recorded in geodetic latitude, longitude, and height. The data were then converted to cartesian coordinates (see Appendix D).

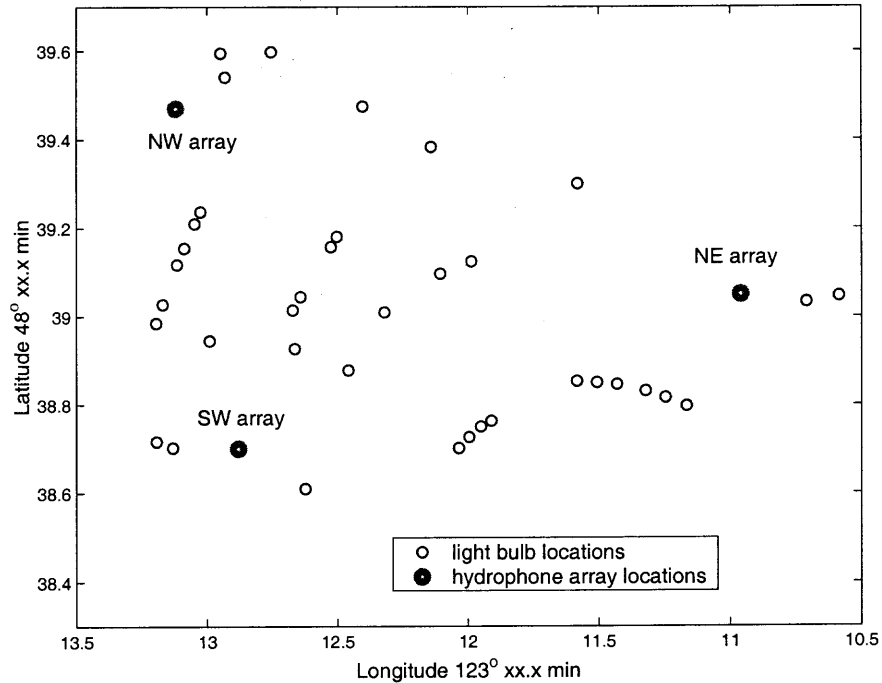


Figure 6.2 Locations of the light bulbs and hydrophone arrays.

6.2.2 NE Data

Figure 6.3 shows the arrival times recorded at the NE-array. Hydrophone 1 represents the shallowest receiver and hydrophone 16 the deepest. For hydrophone 1 to hydrophone 3, the arrivals of the direct ray and the first surface reflected ray overlap. Meanwhile, the arrivals of the first surface reflected ray and the first bottom reflected ray overlap for the hydrophones that are located deeper than hydrophone 8. Therefore, the raw data from hydrophone 4 to hydrophone 8 were used in the linearization process; for these hydrophones, the signal arrivals along the direct, the first surface bounce, and the first bottom bounce, ray paths can be clearly identified.

Source localization is carried out using the linearization method both with least squares and regularization.

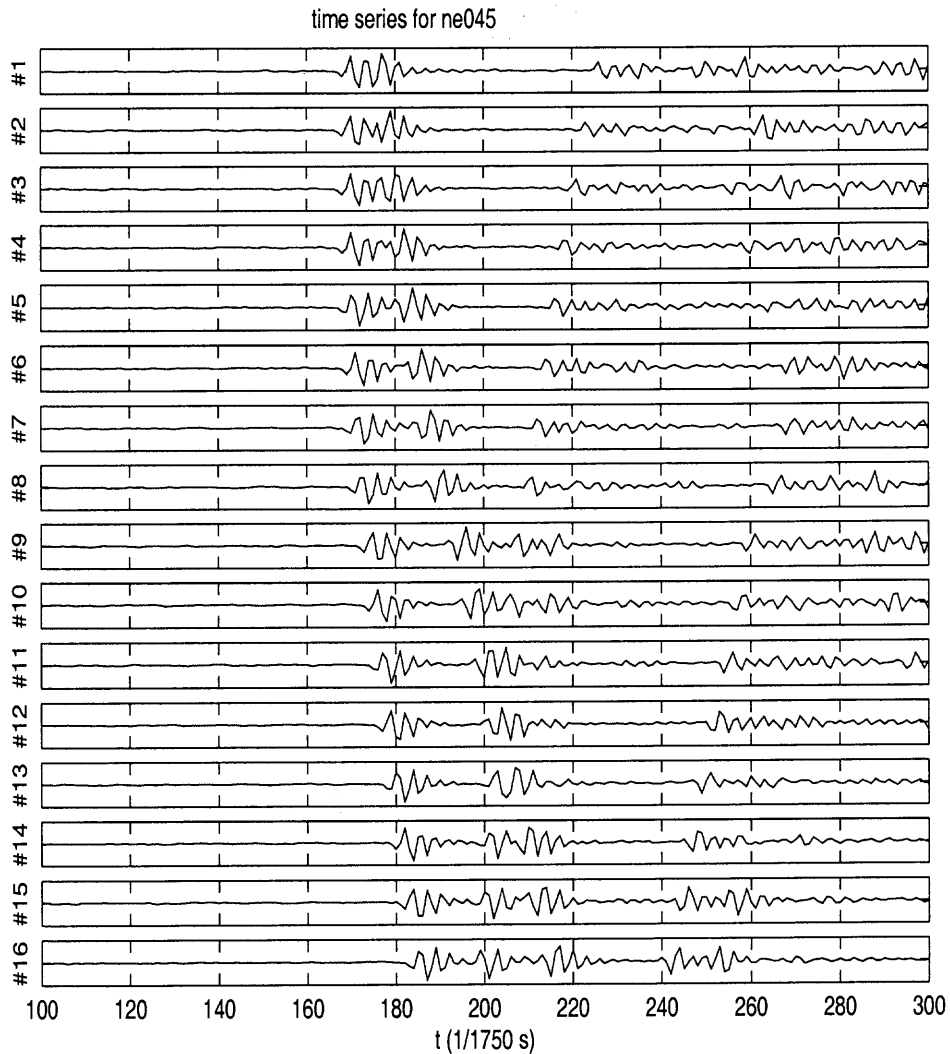


Figure 6.3 Raw light bulb pressure signals, recorded at the NE-array.

1. Least squares inversion:

Table 6.1 shows the inversion results for source range (between source and hydrophone 4), source depth, and bottom depth, assuming that hydrophone depths are known exactly. The inversion results are accurate compared to prior knowledge on source location, with a 5 m difference in source range and a 4 m difference in source depth.

2. Regularization:

As mentioned earlier in this chapter, the hydrophone locations are uncertain.

parameter	reference result (m)	estimated value (m)
r	604.29	609.06
z_s	50.00	46.35
D	150-200	169.60

Table 6.1 Source localization using LS - NE array.

Thus, regularization was applied using the experimental estimated hydrophone depths as a priori information with uncertainties of ± 5 m. The inversion results are shown in Table 6.2.

parameter	reference result (m)	estimated value (m)
r	604.29	607.38
z_s	50.00	46.75
D	150-200	171.53

Table 6.2 Source localization using regularization - NE array.

Unlike the synthetic case, the acoustic inversion of real data from Haro Strait is subject to different errors that make the inversion process more challenging:

- “Low” sampling frequency:

The acoustic data were recorded at a sampling rate of 1750 Hz, which indicates a time step of 0.57 ms between consecutive samples in the time series. This creates ambiguity for arrival time identification, as can be observed from Figure 6.3. In many cases, arrival time differences between adjacent hydrophones along the same ray paths are within or very close to one time step.

- Environmental noise:

background or ambient noise, shipping noise.

Given the presence of these errors, source localization results obtained here using either the least squares method or regularization are very close to the expected source location coordinates. These results are encouraging, indicating the potential of the inversion method for accurate and fast estimation with real data.

6.2.3 NW Data

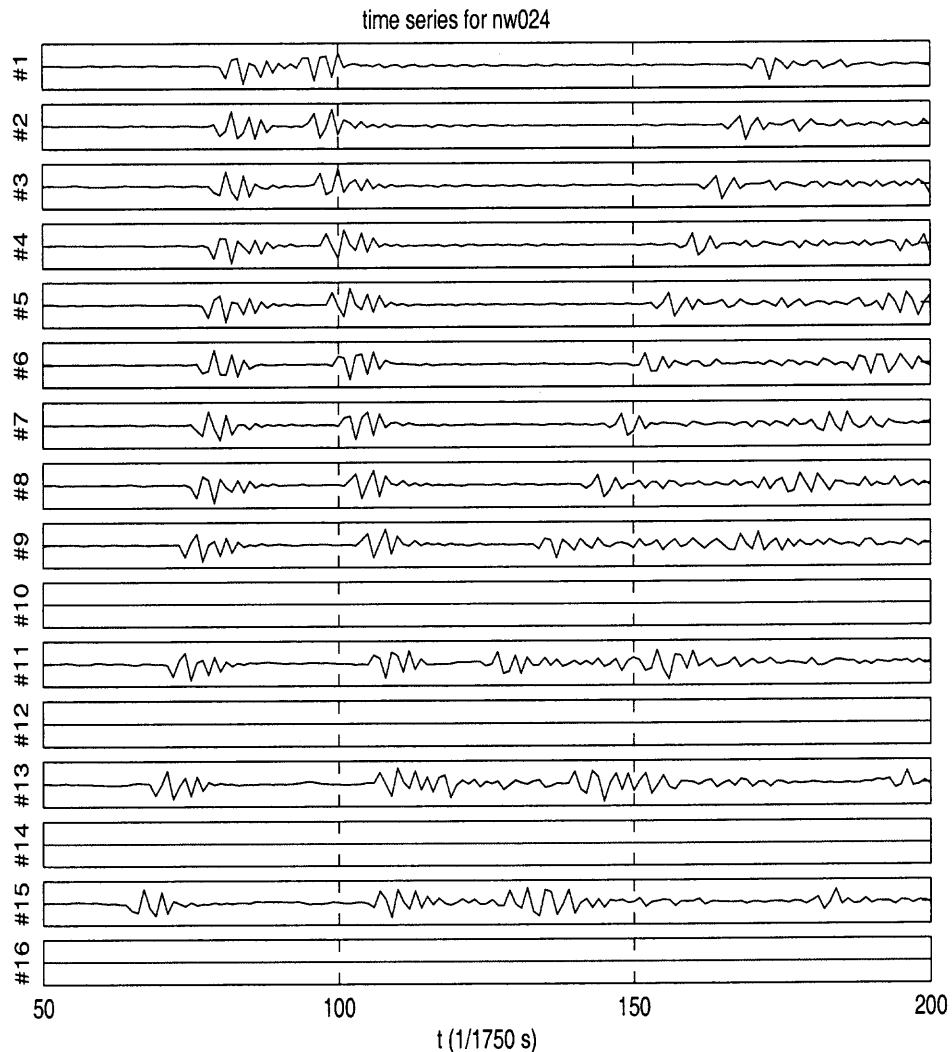


Figure 6.4 Raw light bulb pressure signals, recorded at the NW-array.

Figure 6.4 shows the arrival times recorded at the NW-array. Hydrophones 10, 12, 14, and 16 were not operational in that phase of the experiment. From

hydrophone 1 to hydrophone 9, the arrival times from direct, first surface and first bottom reflected ray paths can be clearly identified. In order to reduce the error level caused by the sampling, hydrophones 1, 3, 5, 7, 9 are chosen for the acoustic inversion. Source localization is carried out using the linearization method with both least squares and regularization in this case as well.

Table 6.3 shows the inversion results from the least squares approach for source range, source depth, and bottom depth; Table 6.4 shows the inversion results using the regularization method.

parameter	reference (m)	estimated value (m)
r	511.60	542.82
z_s	70.00	63.20
D	150-200	206.44

Table 6.3 Source localization using LS - NW array.

parameter	reference (m)	estimated value (m)
r	511.60	509.31
z_s	70.00	60.27
D	150-200	200.45

Table 6.4 Source localization using regularization - NW array.

Source range r denotes the distance between source and hydrophone 1. The inversion results are very good compared to the reference data; results appear to be improved when regularization is employed. These results can be further compared to estimates obtained by Jaschke ([32]), and shown here in Table 6.5.

Jaschke's results were computed using a time matching approach as well. However, Jaschke's method does not employ linearization; instead, he used a Monte Carlo optimization scheme, matching the arrivals of three paths identified from the

parameter	mean (m)	std
r	505.7	4
z_s	60.5	2.5

Table 6.5 Mean and standard deviation of localization parameters from Jaschke's method - NW array.

real data to arrival times of theoretically predicted ray paths for different values of source range and depth. Jaschke's method required arrival time computation for a large number of different source locations in contrast to the linearization scheme which only required few forward model calculations to arrive at almost identical results.

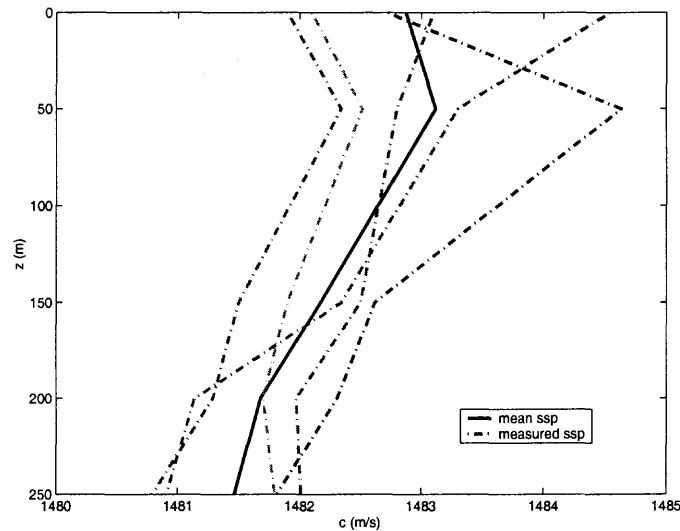


Figure 6.5 "Measured" and mean sound speed profile - NW array.

In the NW case, the regularization method is further applied for sound speed inversion using EOFs. It was assumed that five different profiles were measured and made available. These profiles, presented in Figure 6.5, were obtained by perturbing the reference sound speed of 1482.5 m/s with Gaussian distributed sound speed shifts with zero mean and 2 m/s standard deviation.

The mean sound speed $c_m(z)$ and the eigenvector $v_1(z)$ corresponding to the largest eigenvalue of the excess covariance matrix are then calculated as shown in Table 6.6.

z (m)	$c_m(z)$	$v_1(z)$
0	1482.9	-0.74
50	1483.1	-0.58
150	1482.2	-0.32
200	1481.7	-0.07
350	1481.0	0.05

Table 6.6 Sound speed profile data for sound speed inversion - NW array

To estimate the unknown parameters using regularization, a priori information is taken into account: for the receiver depths, the means are set according to the reference data with 5 m uncertainty; for the bottom depth, the mean is set to 200 m, with 10 m uncertainty; and for the sound speed coefficient, the mean is 0, with uncertainty of 10. Figure 6.6 shows the considered sound speed profiles.

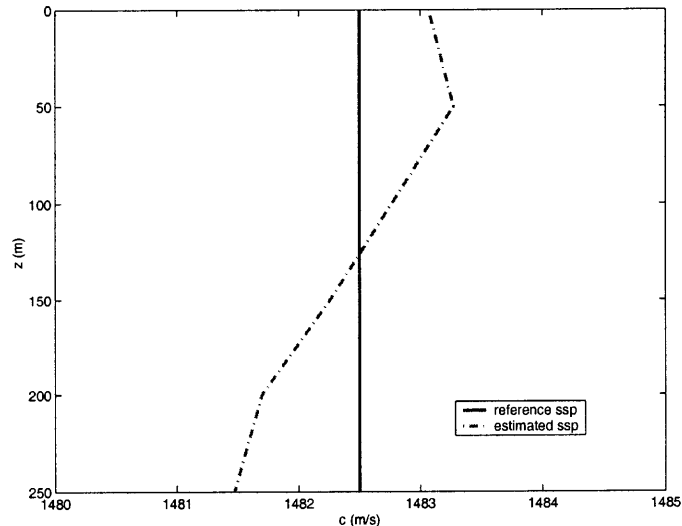


Figure 6.6 Sound speed profile estimation using EOF model.

The inversion results for the sound speed coefficient, along with source range, source depth, and bottom depth are given in Table 6.7. The estimated sound speed

coefficient has a small value, indicating that the true sound speed is actually very close to the originally assumed isovelocity profile.

parameter	reference (m)	estimated value (m)
r	511.60	514.18
z_s	70.00	60.32
D	150-200	202.18
μ		-0.26

Table 6.7 Source localization with uncertain sound speed - NW array.

Finally, estimates for the five receiver depths and ranges (employed during the inversion) are presented in Table 6.8. The differences between the reference values and estimates are within 3 m. As can be observed, the receiver locations follow the general pattern of Figure 6.1, representing the believed array shape.

receiver No.	reference depth (m)	estimated depth (m)	reference range (m)	estimated range (m)
1	52	53.24	511.60	514.18
3	64.49	65.06	511.60	512.52
5	76.95	78.15	511.60	511.98
7	89.32	90.29	511.60	510.17
9	95.47	96.27	511.60	509.18

Table 6.8 Receiver location estimation - NW array.

6.2.4 SW Data

Figure 6.7 shows the arrival times recorded at the SW-array. All hydrophones were operational in the experiment. The receiver hydrophones 3, 5, 7, 9, 11 are employed for source localization, for which the arrival times along three paths (direct, first surface bounce, and first bottom bounce) are clearly separated.

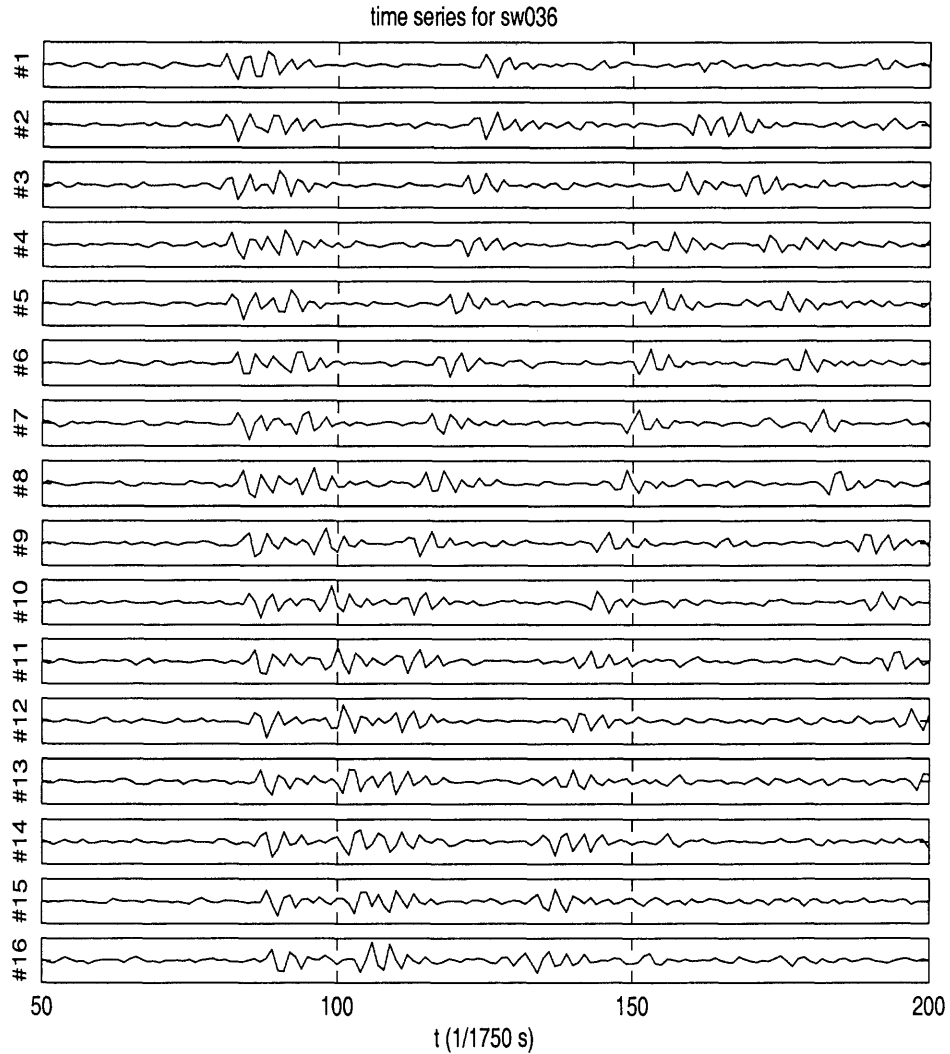


Figure 6.7 Raw light bulb pressure signals, recorded at the SW-array.

Table 6.9 shows the inversion results from the least squares method for source range (between source and hydrophone 3), source depth, and bottom depth; Table 6.10 shows the inversion results using the regularization method.

The source range in this case is much longer compared to the source range in the NE and NW cases. The inversion results are again very close to the reference data.

parameter	reference (m)	estimated value (m)
r	1197.02	1171.78
z_s	50.00	57.74
D	150-200	199.08

Table 6.9 Source localization using LS - SW array.

parameter	reference (m)	estimated value (m)
r	1197.02	1189.25
z_s	50.00	58.08
D	150-200	200.08

Table 6.10 Source localization using regularization - SW array.

CHAPTER 7

MATCHED FIELD INVERSION WITH THE HARO STRAIT DATA

As discussed in the introduction and using the notation of Chapter 2, matched-field processing is an approach that estimates parameters that affect underwater sound propagation by matching the measured field \mathbf{d} to fields predicted with a model \mathbf{f} for different sets of values of the components of vector \mathbf{m} . Conventional matched-field processing is achieved by obtaining an inner product between the measured field at a given frequency and a predicted field (replica) at the same frequency [1]. The inner product is calculated for different vectors \mathbf{m} , generating an ambiguity surface. The vector \mathbf{m} that leads to the maximum value of the ambiguity surface gives the estimates of the unknown parameters.

Broadband matched-field processing can be achieved by calculating and subsequently averaging ambiguity surfaces at several frequencies. Broadband matched-field processing is usually preferable to single frequency matched-field processing because the multiple frequency information helps in the reduction of uncertainty in the estimation process. This uncertainty is especially pronounced in shallow water problems, where sound interacts significantly with the seafloor which is frequently poorly known. If bathymetry, the seafloor structure, and other environmental factors are not modeled properly in the generation of the replica fields, the estimates obtained from matching the true and replica fields can vary substantially from the true values of the unknown parameters.

Matched-field processing was here applied to the Haro Strait data for source localization. It is assumed that the bathymetry is range independent (setting the bottom depth at 200 m). Figure 7.1 shows the environment that was constructed using information from references studying the Haro Strait region [11, 32]. Ambiguity

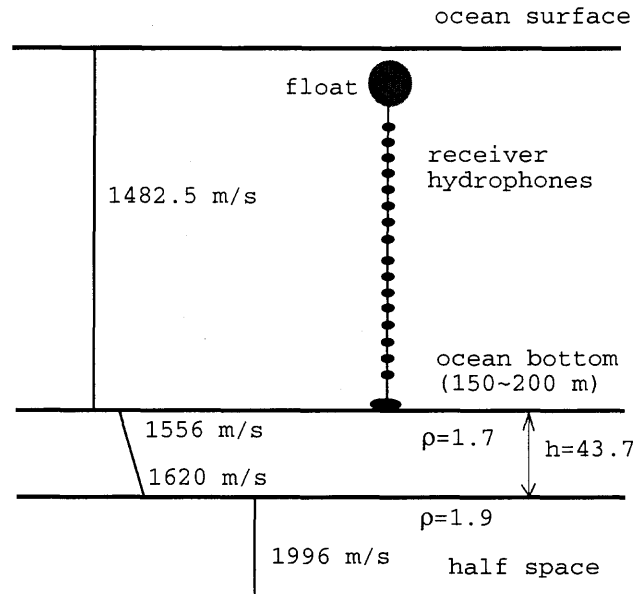


Figure 7.1 Assumed acoustic environment for MFP.

surfaces for each case were computed at 234 frequencies varying between 100 and 800 Hz (the bandwidth of the Haro Strait data) with a 3 Hz spacing. The frequency domain data were generated by applying Fourier transforms to the received time series at the 16 hydrophones (12 phones for the NW data, because four of the phones were not operational in that case). Replica fields were generated using normal modes for the same number of phones and phone locations and for source range varying between 0 and 2 km with a step of 10 m and source depth varying between 0 and 150 m with a step of 3 m.

Figure 7.2 shows a time series received at one of the hydrophones at the NW site and its Fourier transform, demonstrating the frequency content of the received signal.

Figure 7.3 shows the matched-field ambiguity surfaces computed for the three different sites. Dark red areas on the ambiguity surfaces indicate similarity between received and predicted fields; ideally these areas of high similarity should be observed at the region of the correct source location. It can be found that the maxima of the

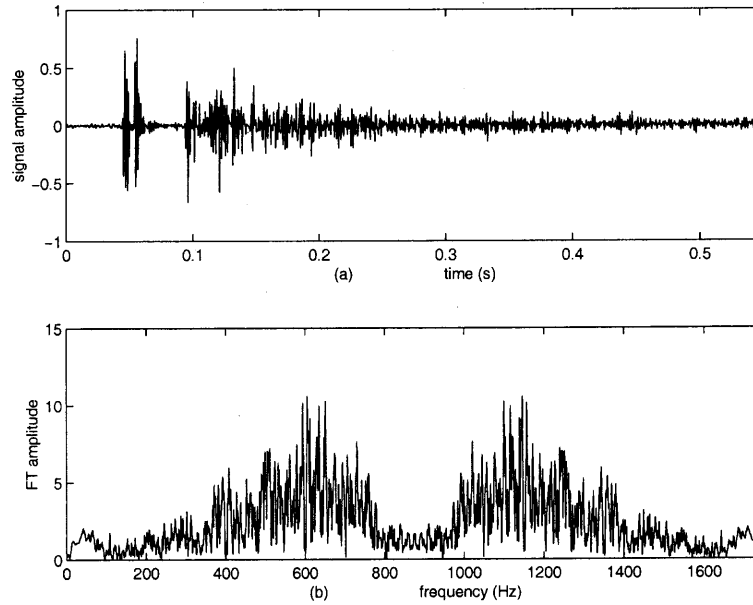


Figure 7.2 Arrival time series recorded in Haro Strait - NW site.

ambiguity surfaces occur at a range and depth of 0.05 km and 150 m for the NW site, 0.06 km and 93 m for the NE site, and 1.19 km and 138 m for the SW site. None of these results are close to the reference value or the localization results obtained with the linearization method. The errors in localization can be attributed to the assumptions involved in generating the replica fields (range independent bathymetry fixed at 200 m, range independent properties of the seafloor sediments, fixed receiver locations).

To perform a more thorough attempt at localization using matched-field processing, optimization with genetic algorithms (SAGA [33]) is also used to invert for the unknown source location for the NW site assuming an uncertain propagation environment. A range independent environment is assumed here as well. In addition to the source location, a search for the bottom depth and the properties of the seafloor is also performed. Localization results for the NW case are 0.36 km and 54 m for range and depth, respectively. The bottom depth was found to be 162 m, and the sediment thickness was estimated at 72.4 m, while an array tilt of

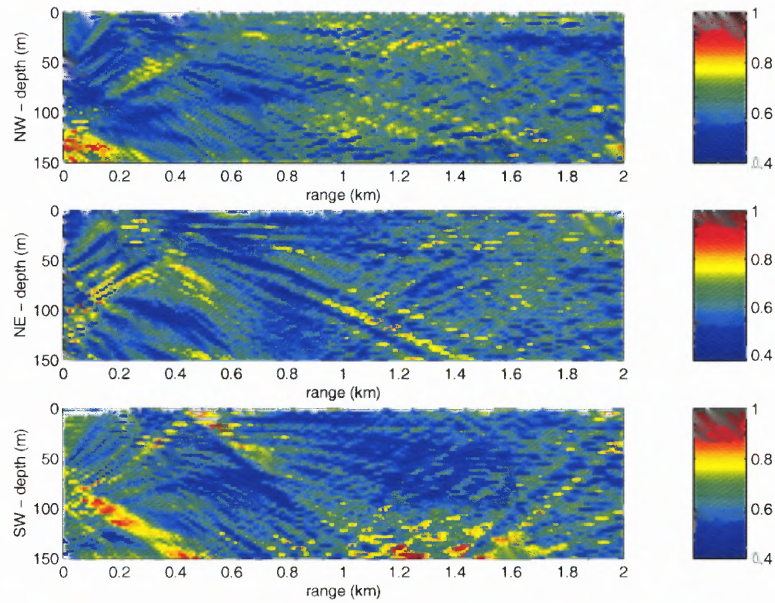


Figure 7.3 Matched-field processing results for three different sites.

1.8° was also calculated. The location estimates are now closer to the true source location; however, the linearization results (Tables 6.3 and 6.4) are much closer to the reference and Jaschke's results. The linearization method was also substantially faster, since it involved a few iterations and derivative calculations. On the other hand, matched-field inversion involved full field modeling using normal modes for a large number of source and receiver locations and values of the environmental parameters.

CHAPTER 8

OCEAN MAMMAL TRACKING

Source tracking in the ocean has been explored from different approaches such as matched-field processing ([34, 35, 36, 37]), optimization with simulated annealing ([38]), or multipath correlation matching ([10]). Most of the source tracking work presented in the literature assumes either constant speed of the source or substantial prior knowledge on the source motion statistics. This chapter focuses on investigating the application of the linearization scheme to source tracking.

8.1 Description of the Tracking Approach

A broadband source is assumed to transmit sound in a shallow water environment (a sperm whale generating clicks, for example). The source moves with a velocity which is unknown and is not assumed to be constant.

The distinct path arrivals are straightforward to identify at the receivers for an impulse-like source function such as a click. Figure 8.1 gives an example of recorded clicks generated by a sperm whale. These clicks are separated by approximately three seconds, an interval larger than the duration of the impulse response of the ocean in the environments that are considered. It is, thus, relatively simple to identify distinct arrivals.

When reception of the signal begins, the arrival times of the direct, first surface bounce, and first bottom bounce paths are identified and compared to arrival times identified on replica paths that would originate from a source at an assumed location. The source location is estimated through the linearization inversion process.

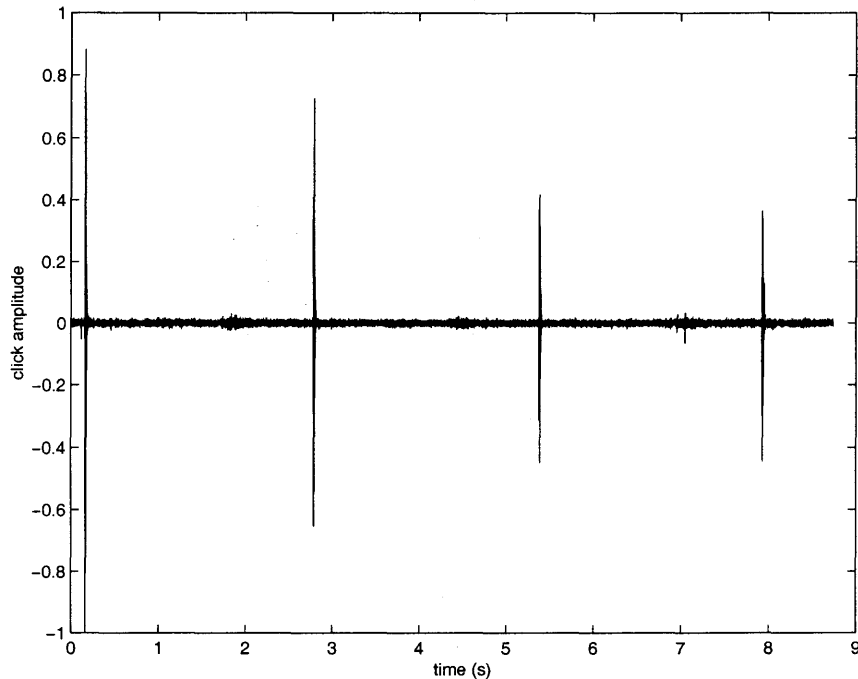


Figure 8.1 Clicks generated from a vocalizing marine mammal (provided by Centro Interdisciplinare di Bioacustica of the University of Pavia, Italy).

When a new signal is detected at the receivers (corresponding to a source that has moved to a new location), the same process is repeated. However, the initial conditions considered are the source location estimates obtained from the previous signal reception. The system solution leads to source location estimates for the second transmission. This procedure is repeated as other new signals are detected. Usually a single iteration is required for convergence at any location after the first.

8.2 Tracking Results Using Synthetic Data

Figure 8.2 shows the true track and one estimated track of the source using the process outlined in the previous section. The tracking results are obtained using relative arrival times with two paths (direct and first surface bounce). Time arrival

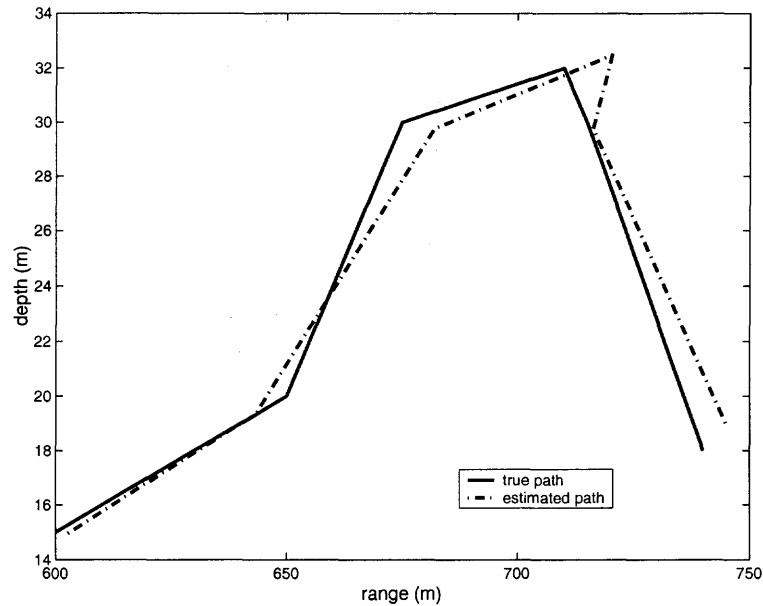


Figure 8.2 Source tracking using relative arrival times with two paths.

uncertainty is represented with zero mean Gaussian distribution with a standard deviation of 0.1 ms.

	two paths	three paths (bottom depth unknown)	three paths (bottom depth known)
range error (m)	8.9	6.9	2.0
depth error (m)	0.5	0.4	0.3

Table 8.1 Rms tracking errors using different paths. The standard deviation for the arrival time uncertainty is 0.1 ms.

Table 8.1 shows the *rms* errors for source range and depth from Monte Carlo simulations of 100 estimated tracks. Different cases are compared including two paths (direct and surface bounce) and three paths (including the first bottom bounce). For the three path situation, two cases are studied including the case of unknown bottom depth which needs to be estimated, and the case in which the bottom depth is exactly known. Results are shown for a standard deviation of 0.1 ms in the arrival time measurements. Localization is successful in all cases; the best estimates

(smallest errors) are obtained when three paths are considered and the bottom depth is known. This result was expected, since the three path with known bottom depth case makes use of more information than the other cases. The second best set of results is obtained when three paths are considered and the bottom depth is unknown. This approach should be preferred over the two-path estimation, when the bottom reflected path can be clearly identified.

	two paths	three paths (bottom depth unknown)	three paths (bottom depth known)
range error (m)	104.2	73.4	16.2
depth error (m)	5.0	3.8	1.4

Table 8.2 Rms tracking errors using different paths. The standard deviation for the arrival time uncertainty is 1 ms.

Tracking results for 1 ms standard deviation in the arrival time uncertainty are shown in Table 8.2. Although errors increase as the noise level becomes higher, estimation of the source location is still good. In the three path with known bottom depth part of the study, errors are quite small, allowing a good understanding of the true motion of the source.

CHAPTER 9

CONCLUSIONS

In this work, an inversion method was developed for source localization of a broadband source in shallow water environments. The method arrives at estimates through a matching process between measured and replica arrival times of different ray paths. The matching is performed with a system, that provides a linear approximation to the inverse process. The system involves derivatives of time with respect to the unknown parameters and is solved using simple least squares or a more sophisticated regularization technique.

The proposed inversion method was initially applied to synthetic data. Several cases were examined, studying the effects of factors such as initial conditions, source instant knowledge, noise in the arrival times, and number of selected paths on the localization results. Also, the sensitivity of those results with respect to uncertainties in bottom depth, receiver location, and sound speed were investigated. The inversion method was found to be accurate and efficient requiring minimal forward model computations. The quality of the inversion improved when prior knowledge on parameters was available and was explored using regularization in the solution of the linear system. With the help of regularization, an inversion scheme was finally implemented inverting for bottom depth, receiver locations, and sound speed along with source location.

Subsequently, inversion using linearization was performed with data collected during the Haro Strait experiment. Results matched reference estimates and were obtained in an efficient manner. Similarly to the simulated data studies, regularization was employed for multiple parameter estimation, including hydrophone and source localization, bottom depth and sound speed estimation. Inversion results were

also obtained for the same data using matched-field processing. The method involved substantial computations and its results differed from the reference values.

Finally, an application of the linearized inversion for tracking broadband sources was presented. The method is ideal for sources such as sperm whales that transmit high frequency broadband signals, generating distinct paths easily identifiable at the receivers.

The method developed in this work can be further extended. It has been applied to near range shallow water problems. Short range and shallow water are not limitations of the technique, however. Addressing problems with further range and/or deeper water would just imply the need for the selection of different paths. The inversion method can be also extended to involve range dependent bathymetry (the necessary time derivatives for a sloping seafloor are presented in Appendix C), and to invert for other parameters such as sound speed and thickness of seafloor sediments.

Although linearized inversion gave excellent inversion results in this work, it can only provide limited information compared to full field matching approaches when used with the appropriate uncertainty modeling. It is here proposed that, when full inversion (source and receiver localization and environmental inversion) is desired, the developed linearized inversion method is used as a preprocessor to an approach such as matched-field processing. The linearized inversion provides accurate information on some of the parameters of interest that can be used to reduce the search space in which matched-field processing will look for the global solution, reducing substantially the computational requirements of the latter approach and improving its estimates.

APPENDIX A

THE DERIVATION OF ARRIVAL TIME DERIVATIVES ALONG RAY PATHS

It is assumed that a given ray travels from medium 1 to medium 2, as shown in Figure A.1, with c_1 and c_2 the sound speeds in each region, and θ_1 and θ_2 the two incident angles in each region. From Snell's Law:

$$\frac{\sin \theta_1}{c_1} = \frac{\sin \theta_2}{c_2}. \quad (A.1)$$

Ray parameter p is introduced, satisfying equation $p = \frac{\sin \theta_i}{c_i}$. From Snell's Law, it can be concluded that p is a constant along each ray path.

Now consider a stack of infinitesimal isovelocity layers:

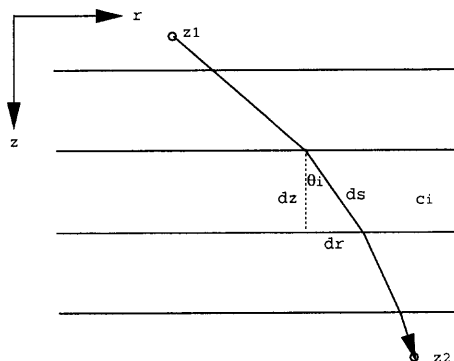


Figure A.1 Sound propagation through infinitesimal isovelocity layers.

For the i^{th} layer, we have

$$\frac{dr}{dz} = \tan \theta_i. \quad (A.2)$$

Along the direct ray path from z_1 to z_2 , range r can be described as

$$r = \int_{z_1}^{z_2} \tan \theta(z) dz. \quad (A.3)$$

From Snell's Law:

$$\sin \theta = pc(z), \quad \cos \theta = \sqrt{1 - p^2 c^2(z)}. \quad (\text{A.4})$$

Equation A.3, thus, leads to:

$$r = \int_{z_1}^{z_2} \frac{pc(z)}{\sqrt{1 - p^2 c^2(z)}} dz. \quad (\text{A.5})$$

Also, since

$$c_i = \frac{ds}{dt} = \frac{dz / \cos \theta_i}{dt}, \quad (\text{A.6})$$

we can write:

$$t = \int_{z_1}^{z_2} \frac{dz}{c(z) \cos \theta(z)} = \int_{z_1}^{z_2} \frac{dz}{c(z) \sqrt{1 - p^2 c^2(z)}}, \quad (\text{A.7})$$

where t is the ray travel time from z_1 to z_2 .

Note that $p = p(r, z_1, z_2)$, that is, p depends on source/receiver locations.

Now the partial derivatives can be derived. These derivatives are needed for travel-time inversion. We start with the derivation of $\frac{\partial t}{\partial z_s}$ along the first surface bounce ray path, where

$$r = \int_0^{z_s} \frac{pc(z)}{\sqrt{1 - p^2 c^2(z)}} dz + \int_0^{z_r} \frac{pc(z)}{\sqrt{1 - p^2 c^2(z)}} dz, \quad (\text{A.8})$$

$$t = \int_0^{z_s} \frac{dz}{c(z) \sqrt{1 - p^2 c^2(z)}} + \int_0^{z_r} \frac{dz}{c(z) \sqrt{1 - p^2 c^2(z)}}. \quad (\text{A.9})$$

From Equation A.9:

$$\begin{aligned} \frac{dt}{dz_s} &= \frac{1}{c(z_s) \sqrt{1 - p^2 c^2(z_s)}} + \\ &\frac{\partial p}{\partial z_s} \left[\int_0^{z_s} \frac{pc(z)}{(1 - p^2 c^2(z))^{3/2}} dz + \int_0^{z_r} \frac{pc(z)}{(1 - p^2 c^2(z))^{3/2}} dz \right]. \end{aligned} \quad (\text{A.10})$$

From Equation A.8:

$$\begin{aligned} \frac{dr}{dz_s} &= \frac{pc(z_s)}{\sqrt{1 - p^2 c^2(z_s)}} + \\ &\frac{\partial p}{\partial z_s} \left[\int_0^{z_s} \frac{c(z)}{(1 - p^2 c^2(z))^{3/2}} dz + \int_0^{z_r} \frac{c(z)}{(1 - p^2 c^2(z))^{3/2}} dz \right]. \end{aligned} \quad (\text{A.11})$$

Note that r and z_s are independent of each other, indicating that $\frac{dr}{dz_s} = 0$. Partial derivative $\frac{\partial p}{\partial z_s}$ can be expressed from Equation A.11 as:

$$\frac{\partial p}{\partial z_s} = \frac{pc(z_s)}{\sqrt{1 - p^2 c^2(z_s)} \left[\int_0^{z_s} \frac{c(z)}{(1 - p^2 c^2(z))^{3/2}} dz + \int_0^{z_r} \frac{c(z)}{(1 - p^2 c^2(z))^{3/2}} dz \right]}. \quad (\text{A.12})$$

Using this result in Equation A.10 and simplifying, the following equation is obtained:

$$\frac{dt}{dz_s} = \frac{\sqrt{1 - p^2 c^2(z_s)}}{c(z_s)}. \quad (\text{A.13})$$

Time derivatives with respect to other parameters along different ray paths can be derived following the same procedure, and the results are shown in Section 3.3.

APPENDIX B

THE DERIVATION OF ARRIVAL TIME DERIVATIVES FOR SOUND SPEED COEFFICIENT

The sound speed profile is described as:

$$\mathbf{c} = \mathbf{c}_m + \mu \mathbf{v}_1 \quad (B.1)$$

where \mathbf{c}_m is the mean sound speed vector, \mathbf{v}_1 is the first eigenvector of the sound speed covariance matrix, and μ is the sound speed perturbation coefficient. Sound speed is modeled as a piece-wise linear function of depth z .

To derive the time derivatives with respect to the sound speed coefficient, we start from the simplest case where $c(z)$ is linear for $z \in [z_{i-1}, z_i]$, and assume $z_{i-1} \leq z_s \leq z_r \leq z_i$.

Given that

$$c(z_{i-1}) = c_{i-1} + \mu v_{i-1}, \quad (B.2)$$

$$c(z_i) = c_i + \mu v_i, \quad (B.3)$$

$c(z)$ can be written as

$$c(z) = \frac{c(z_i) - c(z_{i-1})}{z_i - z_{i-1}} z + \left[c(z_{i-1}) - \frac{c(z_i) - c(z_{i-1})}{z_i - z_{i-1}} z_{i-1} \right]. \quad (B.4)$$

From Equations B.2 and B.3, Equation B.4 results in

$$\begin{aligned} c(z) = & \frac{c_i - c_{i-1}}{z_i - z_{i-1}} z + \frac{z_i c_{i-1} - z_{i-1} c_i}{z_i - z_{i-1}} + \\ & \mu \left[\frac{v_i - v_{i-1}}{z_i - z_{i-1}} z + \frac{z_i v_{i-1} - z_{i-1} v_i}{z_i - z_{i-1}} \right]. \end{aligned} \quad (B.5)$$

Therefore, we have:

$$\frac{\partial c(z)}{\partial \mu} = \frac{v_i - v_{i-1}}{z_i - z_{i-1}} z + \frac{z_i v_{i-1} - z_{i-1} v_i}{z_i - z_{i-1}}. \quad (B.6)$$

To simplify, we define

$$a_{c,i} = \frac{c(z_i) - c(z_{i-1})}{z_i - z_{i-1}}, \quad b_{c,i} = c(z_{i-1}) - a_{c,i}z_{i-1} \quad (B.7)$$

and

$$a_{\mu,i} = \frac{v_i - v_{i-1}}{z_i - z_{i-1}}, \quad b_{\mu,i} = v_{i-1} - a_{\mu,i}z_{i-1}. \quad (B.8)$$

Then:

$$c(z) = a_{c,i}z + b_{c,i}, \quad \frac{\partial c(z)}{\partial \mu} = a_{\mu,i}z + b_{\mu,i}. \quad (B.9)$$

Next, $\frac{dt}{d\mu}$ is derived along the direct ray path. Recall that:

$$t = \int_{z_s}^{z_r} \frac{1}{c\sqrt{1-p^2c^2}} dz, \quad (B.10)$$

Differentiating t with respect to μ , we obtain:

$$\begin{aligned} \frac{dt}{d\mu} &= \frac{\partial t}{\partial c} \frac{\partial c}{\partial \mu} + \frac{\partial t}{\partial p} \frac{\partial p}{\partial \mu} \\ &= \int_{z_s}^{z_r} \frac{(2p^2c^2 - 1)(a_{\mu,i}z + b_{\mu,i})}{c^2(1-p^2c^2)^{3/2}} dz + \frac{\partial p}{\partial \mu} \int_{z_s}^{z_r} \frac{pc}{(1-p^2c^2)^{3/2}} dz. \end{aligned} \quad (B.11)$$

Since:

$$r = \int_{z_s}^{z_r} \frac{pc}{\sqrt{1-p^2c^2}} dz, \quad (B.12)$$

we can write:

$$\begin{aligned} \frac{dr}{d\mu} = 0 &= \frac{\partial r}{\partial c} \frac{\partial c}{\partial \mu} + \frac{\partial r}{\partial p} \frac{\partial p}{\partial \mu} \\ &= \int_{z_s}^{z_r} \frac{p(a_{\mu,i}z + b_{\mu,i})}{(1-p^2c^2)^{3/2}} dz + \frac{\partial p}{\partial \mu} \int_{z_s}^{z_r} \frac{c}{(1-p^2c^2)^{3/2}} dz. \end{aligned} \quad (B.13)$$

Combining Equations B.13 and B.11, $\frac{\partial p}{\partial \mu}$ can be eliminated and we have:

$$\frac{dt}{d\mu} = \int_{z_s}^{z_r} \frac{-a_{\mu,i}z - b_{\mu,i}}{c^2(z)\sqrt{1-p^2c^2(z)}} dz. \quad (B.14)$$

To integrate, we write $\sin \theta = pc(z)$. From Equation B.9:

$$\cos \theta d\theta = a_{c,i} p dz, \quad z = \frac{\sin \theta - pb_{c,i}}{a_{c,i} p}. \quad (\text{B.15})$$

By changing variables, Equation B.14 becomes

$$\begin{aligned} \frac{dt}{d\mu} &= -\frac{p}{a_{c,i}^2} \int \left[\frac{a_{\mu,i}}{p \sin \theta} + \frac{a_{c,i} b_{\mu,i} - a_{\mu,i} b_{c,i}}{\sin^2 \theta} \right] d\theta \\ &= \frac{a_{\mu,i}}{2a_{c,i}^2} \ln \frac{1 - \cos \theta}{1 + \cos \theta} + \frac{p}{a_{c,i}^2} (a_{c,i} b_{\mu,i} - a_{\mu,i} b_{c,i}) \cot \theta. \end{aligned} \quad (\text{B.16})$$

By changing variable θ back to z , we can finally write:

$$\frac{dt}{d\mu} = \frac{a_{\mu,i}}{2a_{c,i}^2} \ln \frac{1 + \sqrt{1 - p^2 c^2}}{1 - \sqrt{1 - p^2 c^2}} + \frac{(a_{c,i} b_{\mu,i} - a_{\mu,i} b_{c,i}) \sqrt{1 - p^2 c^2}}{a_{c,i}^2 c} \Big|_{z_s}^{z_r}. \quad (\text{B.17})$$

When the sound speed profile consists of several linear functions of depth, we obtain:

$$t = \sum_{i=1}^N \int_{z_{i-1}}^{z_i} \frac{1}{c \sqrt{1 - p^2 c^2}} dz, \quad (\text{B.18})$$

$$r = \sum_{i=1}^N \int_{z_{i-1}}^{z_i} \frac{pc}{\sqrt{1 - p^2 c^2}} dz, \quad (\text{B.19})$$

where $c(z)$ is linear $\forall z \in [z_{i-1}, z_i]$, and

$$c(z_i) = c_i + \mu v_i, \quad i = 0, 1, 2, \dots, N. \quad (\text{B.20})$$

Time derivative $\frac{dt}{d\mu}$ is given as:

$$\frac{dt}{d\mu} = \sum_{i=1}^N \frac{a_{\mu,i}}{2a_{c,i}^2} \ln \frac{1 + \sqrt{1 - p^2 c^2}}{1 - \sqrt{1 - p^2 c^2}} + \frac{(a_{c,i} b_{\mu,i} - a_{\mu,i} b_{c,i}) \sqrt{1 - p^2 c^2}}{a_{c,i}^2 c} \Big|_{z_{i-1}}^{z_i} \quad (\text{B.21})$$

where coefficients $a_{c,i}$, $b_{c,i}$, $a_{\mu,i}$, $b_{\mu,i}$ are defined in (B.7) and (B.8).

APPENDIX C

THE DERIVATION OF ARRIVAL TIME DERIVATIVES FOR RANGE DEPENDENT ENVIRONMENT

It is assumed that the ocean has a sloping bottom with constant angle α . Time derivatives with respect to the unknown parameters along the direct and first surface bounce ray paths remain the same as in the independent environment. However, the slope of the bottom has an impact on all derivatives of arrival times of bottom bounce ray paths. In particular, the focus is on the first bottom bounce ray path.

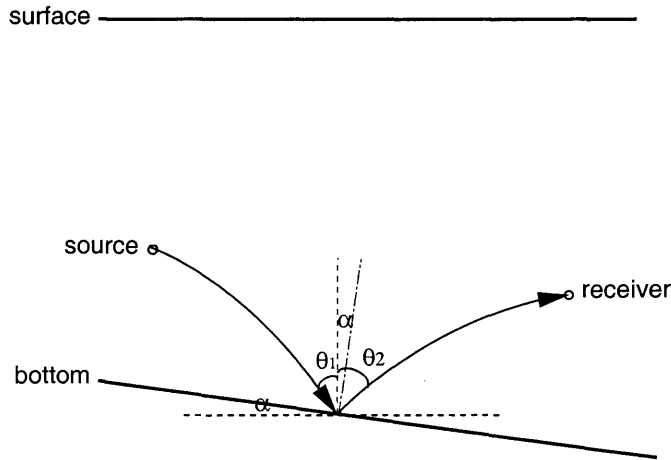


Figure C.1 Bottom bounce ray path in slope bottom case.

Snell's Law still holds in this case, which indicates:

$$p_1 = \frac{\sin \theta_1(z)}{c(z)}, \quad p_2 = \frac{\sin \theta_2(z)}{c(z)}, \quad (C.1)$$

where p_1 and p_2 stand for the ray parameters for each part of the bottom bounce path respectively: from source to bottom, and from bottom to receiver. Angles θ_1 and θ_2 are shown in Figure C.1. At the turning point, the relation between the two angles is described as

$$\theta_2 = \theta_1 + 2\alpha. \quad (C.2)$$

From here, we can derive the relation between the two ray parameters:

$$\begin{aligned} p_2 c(D_T) &= \sin \theta_2 \\ &= \sin(\theta_1 + 2\alpha) \\ &= \cos(2\alpha) \sin \theta_1 + \sin(2\alpha) \cos \theta_1 \\ &= \cos(2\alpha) p_1 c(D_T) + \sin(2\alpha) \sqrt{1 - p_1^2 c^2(D_T)}. \end{aligned} \quad (C.3)$$

From the previous equation:

$$p_2 = \cos(2\alpha) p_1 + \frac{\sin(2\alpha)}{c(D_T)} \sqrt{1 - p_1^2 c^2(D_T)}, \quad (C.4)$$

where D_T is the bottom depth of the site where the ray is reflected from the seafloor.

From Equation C.4,

$$\frac{\partial p_2}{\partial z_s} = \kappa \frac{\partial p_1}{\partial z_s}, \quad (C.5)$$

where z_s is the source depth, and

$$\kappa = \cos(2\alpha) - \frac{\sin(2\alpha) p_1 c(D_T)}{\sqrt{1 - p_1^2 c^2(D_T)}}. \quad (C.6)$$

To derive the time derivative with respect to source depth z_s , we start from the integral expressions for range r and travel time t :

$$t = \int_{z_s}^{D_T} \frac{1}{c(z) \sqrt{1 - p_1^2 c^2(z)}} dz + \int_{z_r}^{D_T} \frac{1}{c(z) \sqrt{1 - p_2^2 c^2(z)}} dz, \quad (C.7)$$

and

$$r = \int_{z_s}^{D_T} \frac{p_1 c(z)}{\sqrt{1 - p_1^2 c^2(z)}} dz + \int_{z_r}^{D_T} \frac{p_2 c(z)}{\sqrt{1 - p_2^2 c^2(z)}} dz. \quad (C.8)$$

Both ray parameters p_1 and p_2 and bottom depth D_T are dependent on z_s ; thus, from Equation C.7 we have:

$$\begin{aligned} \frac{dt}{dz_s} = & -\frac{1}{c(z_s)\sqrt{1 - p_1^2 c^2(z_s)}} + \\ & \frac{\partial p_1}{\partial z_s} \cdot \int_{z_s}^{D_T} \frac{p_1 c(z)}{(1 - p_1^2 c^2(z))^{3/2}} dz + \frac{\partial p_2}{\partial z_s} \cdot \int_{z_r}^{D_T} \frac{p_2 c(z)}{(1 - p_2^2 c^2(z))^{3/2}} dz + \\ & \frac{\partial D_T}{\partial z_s} \left[\frac{1}{c(D_T)\sqrt{1 - p_1^2 c^2(D_T)}} + \frac{1}{c(D_T)\sqrt{1 - p_2^2 c^2(D_T)}} \right]. \end{aligned} \quad (C.9)$$

Assuming that the bottom depth of the receiver position is D_R , from geometry:

$$\tan \alpha = (D_R - D_T)/r_2$$

or

$$r_2 = (D_R - D_T) \cot \alpha, \quad (C.10)$$

where r_2 is defined as the range the bottom bounce ray travels from the reflection point to the receiver. From Equation C.8,

$$r_2 = \int_{z_r}^{D_T} \frac{p_2 c(z)}{\sqrt{1 - p_2^2 c^2(z)}} dz.$$

Equation C.10 can be further expressed as:

$$(D_R - D_T) \cot \alpha = \int_{z_r}^{D_T} \frac{p_2 c(z)}{\sqrt{1 - p_2^2 c^2(z)}} dz. \quad (C.11)$$

From Equation C.11,

$$-\frac{\partial D_T}{\partial z_s} \cot \alpha = \frac{\partial D_T}{\partial z_s} \cdot \frac{p_2 c(D_T)}{\sqrt{1 - p_2^2 c^2(D_T)}} + \frac{\partial p_2}{\partial z_s} \int_{z_r}^{D_T} \frac{c(z)}{(1 - p_2^2 c^2(z))^{3/2}} dz$$

or

$$\frac{\partial D_T}{\partial z_s} = -\frac{\partial p_2}{\partial z_s} \cdot \frac{\int_{z_r}^{D_T} \frac{c(z)}{(1-p_2^2 c^2(z))^{3/2}} dz}{\cot \alpha + p_2 c(D_T) / \sqrt{1-p_2^2 c^2(D_T)}}. \quad (C.12)$$

For simplification, we define I_1 and J_1 as:

$$I_1 = \int_{z_s}^{D_T} \frac{p_1 c(z)}{(1-p_1^2 c^2(z))^{3/2}} dz + \kappa J_1 \int_{z_r}^{D_T} \frac{c(z)}{(1-p_2^2 c^2(z))^{3/2}} dz \quad (C.13)$$

and

$$J_1 = p_2 - \frac{\sqrt{1-p_1^2 c^2(D_T)} + \sqrt{1-p_2^2 c^2(D_T)}}{c(D_T) \sqrt{1-p_1^2 c^2(D_T)} (\cot \alpha \sqrt{1-p_2^2 c^2(D_T)} + p_2 c(D_T))}. \quad (C.14)$$

From Equations C.5 and C.12, Equation C.9 can be written as

$$\frac{dt}{dz_s} = -\frac{1}{c(z_s) \sqrt{1-p_1^2 c^2(z_s)}} + \frac{\partial p_1}{\partial z_s} \cdot I_1. \quad (C.15)$$

Partial derivative $\frac{\partial p_1}{\partial z_s}$ can be obtained from Equation C.8, given that source range and source depth are independent of each other:

$$\begin{aligned} \frac{dr}{dz_s} = 0 = & -\frac{p_1 c(z_s)}{\sqrt{1-p_1^2 c^2(z_s)}} + \frac{\partial p_1}{\partial z_s} \int_{z_s}^{D_T} \frac{c(z)}{(1-p_1^2 c^2(z))^{3/2}} dz + \\ & \frac{\partial D_T}{\partial z_s} \left[\frac{p_1 c(D_T)}{\sqrt{1-p_1^2 c^2(D_T)}} - \cot \alpha \right]. \end{aligned} \quad (C.16)$$

For simplification, we also define I_2 and J_2 as:

$$I_2 = \int_{z_s}^{D_T} \frac{c(z)}{(1-p_1^2 c^2(z))^{3/2}} dz + \kappa J_2 \int_{z_r}^{D_T} \frac{c(z)}{(1-p_2^2 c^2(z))^{3/2}} dz \quad (C.17)$$

and

$$J_2 = \frac{\sqrt{1-p_2^2 c^2(D_T)} (\cot \alpha \sqrt{1-p_1^2 c^2(D_T)} - p_1 c(D_T))}{\sqrt{1-p_1^2 c^2(D_T)} (\cot \alpha \sqrt{1-p_2^2 c^2(D_T)} + p_2 c(D_T))}. \quad (C.18)$$

From Equations C.5 and C.12, Equation C.16 can be written as

$$\frac{\partial r}{\partial z_s} = 0 = -\frac{p_1 c(z_s)}{\sqrt{1-p_1^2 c^2(z_s)}} + \frac{\partial p_1}{\partial z_s} \cdot I_2. \quad (C.19)$$

From Equation C.19, $\frac{\partial p_1}{\partial z_s}$ can be obtained and used in Equation C.15. Finally, we have

$$\frac{dt}{dz_s} = -\frac{1}{c(z_s)\sqrt{1-p_1^2c^2(z_s)}} + \frac{p_1c(z_s)}{\sqrt{1-p_1^2c^2(z_s)}} \cdot \frac{I_1}{I_2}. \quad (C.20)$$

Following similar procedures, other time derivatives can be derived.

APPENDIX D

COORDINATES CONVERSION BETWEEN GEODETIC SYSTEM AND CARTESIAN SYSTEM

The transform from geodetic to cartesian coordinates is performed as follows ([39]):

$$X = (N + h) \cos \phi \cos \lambda,$$

$$Y = (N + h) \cos \phi \sin \lambda,$$

$$Z = (N(1 - e^2) + h) \sin \phi,$$

where:

ϕ : geodetic latitude

λ : geodetic longitude

h : height

X, Y, Z : cartesian coordinates

a : Equatorial Radius (6378137.0 m)

b : Polar Radius (6356752.3142 m)

N : radius of curvature in prime vertical $= a / \sqrt{1 - e^2 \sin^2 \phi}$

e^2 : eccentricity squared $= 2f - f^2$

f : flattening $= (a - b) / a$.

REFERENCES

1. A. Tolstoy, *Matched Field Processing for Underwater Acoustics*, World Scientific, 1993.
2. M. B. Porter and A. Tolstoy, “*The matched field processing benchmark problems*”, *Journal of Computational Acoustics*, 2(3), pp. 161–185, 1994.
3. B. Baggeroer, William A. Kuperman, and Peter N. Mikhalevsky, “*An overview of matched field methods in ocean acoustics*”, *IEEE Journal of Oceanic Engineering*, 18(4), pp. 401–424, 1993.
4. A. Tolstoy, “*Simulated performance of acoustic tomography via matched field processing*”, *Journal of Computational Acoustics*, 2(1), pp. 1–10, 1994.
5. Z.-H. Michalopoulou and M. B. Porter, “*Localization in the Gulf of Mexico*”, *IEEE Workshop on Underwater Acoustics Signal Processing*, 1995.
6. Zoi-Heleni Michalopoulou and Michael B. Porter, “*Matched-field processing for broad-band Source localization*”, *IEEE Journal of Oceanic Engineering*, 21(4), 384–392, 1996.
7. Zoi-Heleni Michalopoulou and Michael B. Porter, “*Source tracking in the Hudson Canyon*”, *Journal of Computational Acoustics*, 1996.
8. E. K. Westwood, “*Broadband matched-field source localization*”, *J. Acoust. Soc. Am.*, 91, pp. 2777–2789, 1992.
9. A. Baggeroer, W. Kuperman, and H. Schmidt, “*Matched field processing: Source localization in correlated noise as an optimum parameters estimation problem*”, *J. Acoust. Soc. Am.*, 83, pp. 571–587, 1988.
10. Evan K. Westwood and David P. Knobles, “*Source track localization via multipath correlation matching*”, *J. Acoust. Soc. Am.*, 102(5), pt. 1, pp. 2645–2654, 1997.
11. Patrick Pignot and Ross Chapman, “*Tomographic inversion for geoacoustic properties in a range dependent shallow water environment*”, *J. Acoust. Soc. Am.*, 104 (3), 1998.
12. Sergio M. Jesus, Michael B. Porter, Yann Stephan, Xavier Demoulin, Orlando C. Rodriguez, and Emanuel M. M. Ferreira Coelho, “*Single hydrophone source localization*”, *IEEE Journal of Oceanic Engineering*, 25(3), pp. 337–346, 2000.
13. Stan. E. Dosso, Mark. R. Fallat, Barbara. J. Sotirin, and John L. Newton, “*Array element localization for horizontal arrays via Occam’s inversion*”, *J. Acoust. Soc. Am.*, 104 (2), pp. 846–859, 1998.

14. A. Tolstoy, “*Linearization of the matched field processing approach to acoustic tomography*”, J. Acoust. Soc. Am., 91 (2), pp. 781–787, 1992.
15. A. Tolstoy, “*Tomographic inversion for geoacoustic parameters in shallow water*”, Journal of Computational Acoustics, 8(2), pp. 285–293, 2000.
16. Stan. E. Dosso, Gary. H. Brooke, Steven J. Kilistoff, Barbara J. Sotirin, Vincent K. McDonald, Mark R. Fallat, and Nicole E. Collison, “*High-precision array element localization for vertical line arrays in the Arctic Ocean*”, IEEE Journal of Oceanic Engineering, 23(4), pp. 365–379, 1998.
17. A. Tarantola, *Inverse Problem Theory*, Elsevier, 1987.
18. W. Menke, *Geophysical Data Analysis: Discrete Inverse Theory*, Academic Press, 1989.
19. Finn B. Jensen, William A. Kuperman, Michael B. Porter, and Henrik Schmidt, *Computational Ocean Acoustics*, AIP Press, 1994.
20. Ivan Tolstoy and C. S. Clay, *OCEAN ACOUSTICS: Theory and Experiment in Underwater Sound*, American Institute of Physics, Inc., 1987.
21. George V. Frisk, *OCEAN AND SEABED ACOUSTICS: A Theory of Wave Propagation*, P T R Prentice Hall, 1994.
22. Michael B. Porter, *The KRAKEN normal mode program*, 1991.
23. J. Douglas Faires and Richard L. Burden, *Numerical Methods*, PWS-KENT Publishing Company, 1993.
24. Gilbert Strang, *Linear Algebra and Its Application*, Sanders HBJ, 1988.
25. William H. Press, Saul A. Teukolsky, William T. Vetterling, and Brian P. Flannery, *Numerical Recipes in C, The Art of Scientific Computing*, Cambridge University Press, 1999.
26. A. Scales, P. Docherty, and Adam Gersztenkorn, “*Regularization of nonlinear inverse problems: imaging the near-surface weathering layer*”, Inverse Problems 6, pp. 115–131, 1990.
27. Zoi-Heleni Michalopoulou, “*Matched-impulse-response processing for shallow-water localization and geoacoustic inversion*”, J. Acoust. Soc. Am., 108 (5), pp. 2082–2090, 2000.
28. Robert C. Spindel, “*Signal processing in ocean tomography*”, H. G. Urban, Adaptive Methods in Underwater Acoustics, pp. 687–710, 1985.
29. Walter Munk and Carl Wunsch, “*Ocean acoustic tomography: A scheme for large scale monitoring*”, Deep-Sea Research, 26, pp. 123–161, 1979.

30. Jean-Pierre Hermand, "*Broad-band geoacoustic inversion in shallow water from waveguide impulse response measurements on a single hydrophone: theory and experimental results*", IEEE Journal of Oceanic Engineering, 24(1), pp. 41–66, 1999.
31. L. R. LeBlanc and F. H. Middleton, "*An underwater acoustic sound velocity model*", J. Acoust. Soc. Am., 67(6), pp. 2055–2062, 1980.
32. Lothar Jaschke, "*Geophysical inversion by the freeze bath method with an application to geoacoustic ocean bottom parameter estimation*", Master's Thesis, University of Victoria, 1997.
33. P. Gerstoft, "*SAGA Users guide 2.0, an inversion software package*", SACLANT Undersea Research Centre, SM-333, La Spezia, Italy, 1997.
34. Homer Bucker, "*Matched-field tracking in shallow water*", J. Acoust. Soc. Am., 96 (6), 1994.
35. Homer Bucker, "*Least-squares target detection for a twin-line towed array*", J. Acoust. Soc. Am., 95 (3), 1994.
36. John A. Fawcett and Brian H. Maranda, "*A hybrid target motion analysis/matched-field processing localization method*", J. Acoust. Soc. Am., 94 (3), 1993.
37. Stacy L. Tantum and Loren W. Nolte, "*Tracking and localizing a moving source in an uncertain shallow water environment*", J. Acoust. Soc. Am., 103(1), pp. 362–373, 1998.
38. Brian H. Maranda and John A. Fawcett, "*Localization of a maneuvering target using simulated annealing*", J. Acoust. Soc. Am., 94 (3), pt. 1, 1993.
39. George P. Gerdan and Rodney E. Deakin, "*Transforming cartesian coordinates X, Y, Z to geographical coordinates ϕ, λ, h* ", The Australian Surveyor, 44(1), 1999.